A Diamond Nanomembrane Detector for Proteomics

By

Hyunseok Kim

A dissertation submitted in partial fulfillment of

the requirements for the degree of

Doctor of Philosophy

(Electrical Engineering)

at the

UNIVERSITY OF WISCONSIN-MADISON

2014

Date of final oral examination: 05/08/14

The dissertation is approved by the following members of the Final Oral Committee:

Robert H. Blick, Professor, Electrical Engineering

Zhenqiang Ma, Professor, Electrical Engineering

Luke J. Mawst, Professor, Electrical Engineering

Max G. Lagally, Professor, Materials Science and Engineering

Thomas Rockwell Mackie, Professor Emeritus, Medical Physics

Abstract

Mechanical resonators realized on the nanoscale by now offer applications in mass sensing of bio-molecules with extraordinary sensitivity [19-21]. The general idea is that perfect mechanical mass sensors should be of extremely small size to achieve zepto- or yocto-gram sensitivity in weighing single molecules similar to a classical scale. However, the small effective size and long response time for weighing biomolecules with a cantilever restricts their usefulness as a high-throughput method. Commercial mass spectrometry (MS) on the other hand, such as electro-spray ionization (ESI)-MS and matrix-assisted laser desorption/ionization (MALDI)-time of flight (TOF)-MS and their charge amplifying detectors are the gold standards to which nanomechanical resonators have to live up to. These two methods rely on the ionization and acceleration of biomolecules and the following ion detection after a mass selection step, such as time-of-flight (TOF). Hence, mass spectra are typically represented in *m/z*, i.e. the mass *m* to ionization charge ratio *z*. The principle we are describing here for ion detection is based on conversion of kinetic energy of the biomolecules into thermal excitation of CVD diamond nanomembranes via phonons, followed by phonon-mediated detection via field emission of thermally emitted electrons. We fabricated ultrathin diamond membranes with extreme aspect ratios for MALDI-TOF MS of high mass proteins. These diamond membranes are realized by straightforward etching methods based on semiconductor processing. Ion detection is demonstrated in MALDI-TOF analysis over a broad range of

proteins from Insulin to BSA. The resulting data and numerical calculations for detection with diamond nanomembranes offer the better sensitivity and overall performance in resolving protein masses as compared to existing detectors.

Acknowledgements

I have many people who I would like to thank. I could be able to successfully perform the Ph.D program with their great supports and advices. I would like to show my appreciations to those people who helped me to complete my thesis research.

First of all, I thank my Ph.D advisor, Professor Robert H. Blick for providing me valuable advices in research projects through the graduate years. He is an advisor who does not judge a student based on the previous background, but gives equal chances to his students and evaluates them based on efforts in tasks they are performing. He provided many opportunities for me without backgrounds in NEMS/MEMS area to study and perform various research projects so that I could have great research and academic experiences in that area. All the projects initiated from his creative idea were exciting and challenging to me so that I could build ability for solving the problems and applying new concepts.

I thank Professor Thomas Rockwell Mackie for his financial and academic support during two year research collaboration in the biomedical system under WARF grant. He gave great advices and discussion in every research meeting. He suggested good ways and creative ideas about how the project should go and the problems can be solved. He also provided many valuable comments in my thesis and defense.

I thank Professor Max G. Lagally for his financial support and advices under MURI grant. With his support, I could have a lot of cleanroom experience in making

freestanding nanomembranes for protein mass detection and build some setups for experiment.

I thank Professor Lloyd M. Smith for his financial support and advices under NIH grant during my final graduate year. Without his support, I could not be able to continuously perform the research project for application of diamond nanomembrane detectors to mass spectrometry. He cared me with financial support to the end of graduation and provided academic and personal advices to me.

I thank Dr. Zlatan Aksamija for numerical calculation included in my thesis. He performed final modeling and simulation for the output response via phonon-assisted field emission and heat flux after the high impact energy ion packet bombardment deposits its thermal energy on the backside of diamond nanomembranes. He helped me obtain deep theoretical knowledge and explain physical phenomena behind diamond nanomembranes through continuous discussions.

I thank many people including former and current group members in the lab., Dr. Hyun-Seok Kim, Dr. Chulki Kim, Dr. Minrui Yu, Dr. Eric Stava, Dr. Hyuncheol (Caleb) Shin, Dr. Dustin Kreft, Dr. Jonghoo Park, Hyun-Cheol Shin, Abhishek Bhat, Jonathan Rodriguez, Mo Zhao, and Arjun Seshadri. Specially, Dr. Jonghoo Park gave assistance to my system setups and experiment via continuous discussions. Hyun-Cheol Shin gave me a hand with assembling measurement systems and preparing protein samples. I also thank Dr. Diana Hildebrand from University of Hamburg (Germany) and Ranran Liu from Professor Smith’s group.

I thank my parents, my parents in law, my younger sister, and younger brother in

law. They supported me during all graduate years with cheering advices and encouragement. My father and mother continuously show their love for me and lead me not giving up during the hard time in my life. My mother in law always cheers me up so that I can overcome any difficulty in life. At this time, I specially recall the memory about my father in law who passed away four years ago and cannot see my completion of Ph.D dissertation. He cared me with hearty advices and encouragement to the moment of the end in his life. Without their prayer and support for me, I could not be able to successfully complete the Ph.D program.

I thank my wife, Taena Kim. She has always been with me through the life in U.S.A. She always shows her love for me and encourages me with wholehearted advices and prayer. Without her love and trust for me, I could not be able to achieve completion of my degree. As like by now, she will share my life forever as my supporter and lovely companion. I thank my lovely and cute daughter, Aine Kim. She is always lifeblood to me. With seeing her cute tricks and her growing well, I could recover from fatigue with work and frustration in the hard time. I love you so much, Taena and Aine.

I always thank God. He is always the lighthouse and a milestone for me in my whole life. He always leads me to good way he already planned for me. He does not let me down during the most difficult time. I believe that I could be able to successfully finish my degree under his care and help as the biggest supporter. I believe that he will guide me to his way for me and use my talent for his purpose.

Table of Contents

List of Figures

List of Tables

Chapter 1

Introduction

In this chapter general mass spectrometry and technologies are first introduced with individual characteristics of each mass spectrometry system. Recent research efforts for enhancing performance of sensitive detection of protein masses are then presented. Limitations of commercial detectors are also discussed in efficiency, sensitivities, reliability, and applicability. The principle of MALDI-TOF Mass spectrometry (MS) as an effective system for mass spectrometry is introduced. Several recent approaches based on nanomembrane MALDI-TOF MS are discussed in terms of principles, performance, and limitation. Finally, the motivation of this research is discussed in terms of diamond being a nanomembrane detector material with excellent physical, chemical, and electrical properties.

1.1 Mass Spectrometry

Proteomics is the study of the proteome which is the entire set of proteins, produced or modified by an organism or system. Proteomics has evolved from genomics (human genome project) sequencing DNA since the static set of genes cannot properly explain the continuous changes of proteins according to condition and environment of

organisms time to time. Proteomics focuses on the identification, localization, and functional analysis of the protein make-up of the cell. Proteins are vital parts of living organisms, as they are the main components of the physiological metabolic pathways of cells. When pathogens infect the human body, causing disease, proteins play a key role in signaling the presence and ridding it of these invaders. Due to the high degree of complexity of cellular proteomes and the low abundance of many proteins, a highly sensitive analytical technology is required. Mass spectrometry has increasingly become the method of choice for analysis of complex protein samples now available due to genome sequence databases and the technical advances.

1.1.1 Mass spectrometry and technologies

A mass spectrometer generates multiple ions from the sample under investigation, separates them according to their specific mass-to-charge ratio (m/z), and then records the relative abundance of each ion type. The first step in the mass spectrometric analysis of compounds is the production of gas phase ions of the compound, basically by electron ionization. This molecular ion undergoes fragmentation. Each primary product ion derived from the molecular ion, in turn, undergoes fragmentation, and so on. The ions are separated in the mass spectrometer according to their mass-to-charge ratio, and are detected in proportion to their abundance. A mass spectrum of the molecule is thus produced. It displays the result in the form of a plot of ion abundance versus mass-to-charge ratio. Ions provide information concerning the nature and the structure of their precursor molecule.

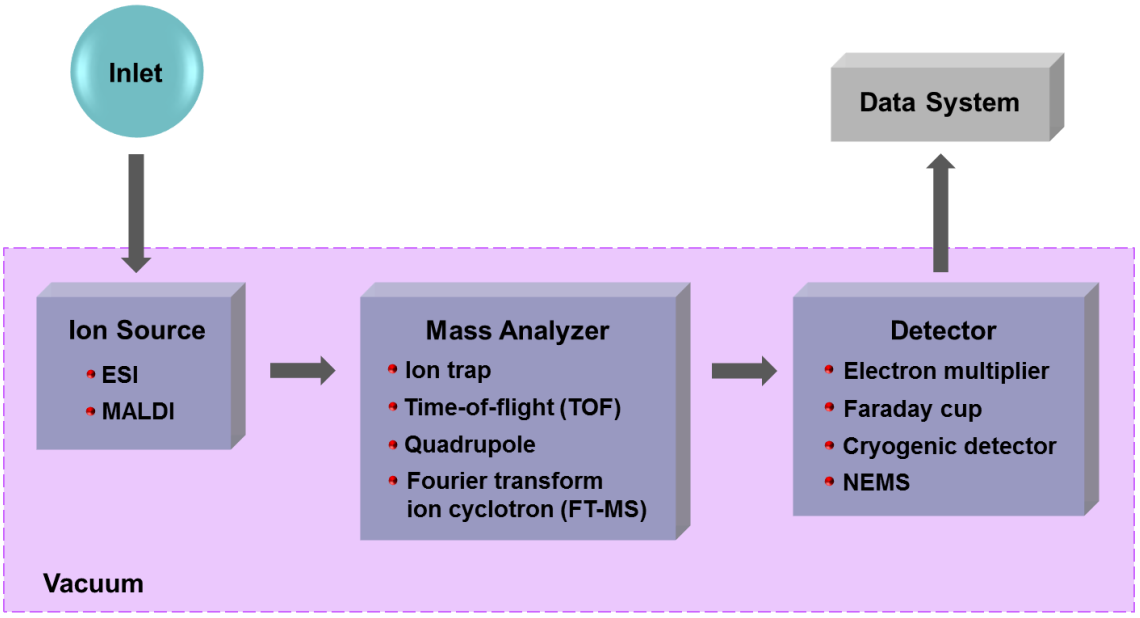

Fig. 1-1 Simplified schematic of Mass spectrometry and technologies

Mass spectrometry consists of three main components as shown in Fig. 1-1: an ion source, which produces gaseous ions from the substance being studied; a mass analyzer, which resolves the ions into their characteristics mass components according to their mass-to-charge (*m/z*) ratio; and a detector, which detects the ions at each *m/z* value. Electronspray ionization (ESI) and matrix-assisted laser desorption/ionization (MALDI) are the two technologies most commonly used to volatize and ionize the proteins or peptides for mass spectrometric analysis [1-3]. ESI ionizes the analytes out of a solution. Therefore, it is readily coupled to liquid-based separation tools. MALDI which is the most notable protein ionization method as recognized by the 2002 Nobel Prize in chemistry [1] ionizes the samples from the dry and crystalline matrix via laser pulses.

The mass analyzer plays a crucial role in mass spectrometry. Its key parameters are sensitivity, resolution, and mass accuracy [1, 4]. There are four basic types of mass

analyzers currently used in MS: ion trap [5], time-of-flight (TOF) [6-8], quadrupole [9], and Fourier transform ion cyclotron (FT-MS) analyzers [10, 11]. In ion trap analyzers, the ions are first captured or trapped for a certain time interval before the actual analysis. This type of mass spectrometer is extremely fast, but offers low resolution and low mass accuracy due to the limited number of ions that can be accumulated [1]. MALDI is usually coupled to TOF analyzers that measure the mass of intact sample ions, whereas ESI has mostly been coupled to ion traps and triple quadrupole instrument for generating fragment ion spectra of selected precursor ions [1]. In a quadrupole mass spectrometer, the quadrupole is the component of the instrument for filtering sample ions based on their *m/z* ratio. Ions are separated in a quadrupole based on the stability of their trajectories in the oscillating electric field applied to the rods. This type of mass spectrometer possesses good reproducibility and requires relatively small and low-cost setups, while the system is not well suited for the commonly used pulsed-ionization methods and the performance depends strongly on energy, collision gas, and pressure. FT-MS instrument also traps ions in a high magnetic field where each ion has a characteristic cyclotron frequency of oscillation that can be related to its *m/z* ratio. It measures *m/z* by detecting the cyclotron frequency produced by the trapped ions. A mass spectrum is extracted from the signal using a Fourier transform. This type of mass spectrometer offers high sensitivity and resolution, but it operates relatively slow and requires expensive maintenance [1].

As a result of its simplicity, high speed, highest practical mass ranges, excellent mass accuracy, high resolution, and sensitivity, MALDI-TOF is still the method of choice for identifying peptides and proteins.

The detectors are important parts for enhancing the performance of MS in terms of resolution, sensitivity, and life time. The parts of ion source and mass analyzer are getting well developed with overall high performances nowadays. However, little has changed on the detector side of MS. Basically three different detection methods are used [12]: direct charge detection (in the Faraday cup detector), image charge detection (in inductive detector), or secondary electron generation (in the electron multiplier (EM) or microchannel plate (MCP) detector). Among those detectors, the electron multiplier (EM) or microchannel plate (MCP) satisfies the requirements such as large area for permitting spatial extent of ions, response time resolution, and sensitivity. In these detectors, the incident ions generate secondary electrons by attacking the surface, followed by amplifying the signal via a sequential cascade processe of electrons inside the detectors to the magnified output signal. The detectors have large active areas and rapid response times. Specially, for smaller and fast moving ions (e.g. relatively low m/z ions less than 1,000 Daltons (Da)), the detectors are highly sensitive and effective with high conversion efficiency of incident ions to secondary electrons.

However, these detectors suffer from the primary obstacle of dramatically decreased sensitivity with increasing m/z in analysis of large mass ions such as DNA molecules and proteins produced in the MALDI process as shown in Fig. 1-2(a). It is evident from this figure that the ion signal obtained from the higher mass components (it means larger time-of-flight and lower velocity) is much smaller than that obtained from the lower mass components. In terms of secondary electron yield considering secondary electron emission efficiency which is defined as the probability for emitting one or more

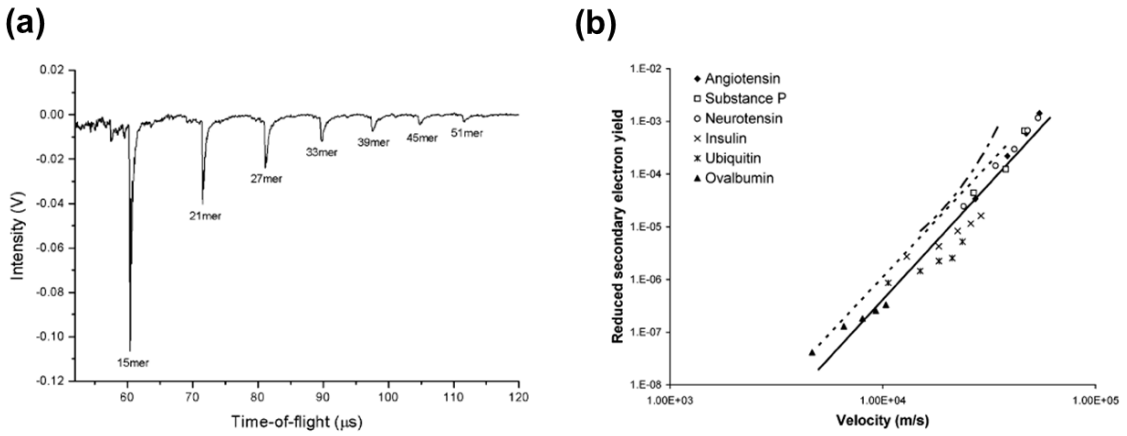

Fig. 1-2 Decreased sensitivity in output signal of MCP detector with increasing mass of ions. (a) MALDI-TOF MS analysis of an equimolar (5 μM) mixture of seven oligonucleotides showing a decrease in signal intensity with increasing mass. (b) Reduced secondary electron yield, γ_e/m, of the MCP for protein ions. The solid line is a fit to the data using the function, $\gamma_e/m=Av^B$, where $A=10^{-24\pm1}$ and $B=4.4\pm0.2$ [13].

electrons from the impact of an incident ion, the reduced secondary electron yield (shown in Fig. 1-2(b)), γ_e/m is changed as the function of $v^{4.4}$ which means that the heavier ions move through the flight tube more slowly, leading to large decrease in ion detection efficiency as shown in Fig. 1-2(a). The effect of detection saturation contributes also small parts to the source of the signal loss.

These phenomena give extreme limitation to the ability of mass spectrometric method for analysis in large mass DNA or proteins which get demands at the areas of proteomics and clinical applications. In order to extend the mass range to larger molecules, the development of more sensitive and enhanced detectors is necessary.

Cryogenic microcalorimeter is one of the types in detector as shown in Fig. 1-1. These detectors [14, 15] are operated at the temperature of 4K with giving very high detection efficiency, low noise levels, and performance of single ion counting by

measuring the amount of kinetic energy deposited in the detector by the ion impact. However, the cryogenic microcalorimeter has some limitations in mass spectrometry due to a few existence of the systems in the world, little development by now, a little research in those areas, high cost maintenance, relatively long response time (e.g. order of microseconds), and limited energy resolution [16].

More recently, several researches have been performed for detection of ions by using resonance frequency shifting via ion adsorption on the surface of nanoelectromechnical systems (NEMS) resonator [17-19]. Resonance frequencies can be described as the function of mass in the device. Small mass changes by ion adsorption on the device cause resonance frequency shift of total device, followed by calculation of mass changes via the amount of frequency shift. Theoretically, the mass below a single Dalton (1 Dalton = 1.66×10^{-27} kg) is achievable in physically realizable devices. NEMS-based mass spectrometry has been realized for detecting ions with coupling to ESI and MALDI used as ion sources [20, 21]. Their approaches are quite distinct in that the inertial mass of each molecule is weighed as the analyte adsorbs on the resonator. Those systems do not use a mass analyzer for pre-separating the molecule. Instead, real-time monitoring of the resonance frequency shift is performed to distinguish the mass of ions attached onto the surface of the devices at a given time. Using this method, BSA (66 kDa) and β–amylase (200 kDa) were detected [20]. Most recently, NEMS-based detection of ions with much higher mass such as gold particles (~4 MDa) and human immunoglobulin M (IgM, ~1 MDa) was shown using both ESI and MALDI [21]. Although this approach has demonstrated high mass sensitivity, the devices suffer from low active area and slow

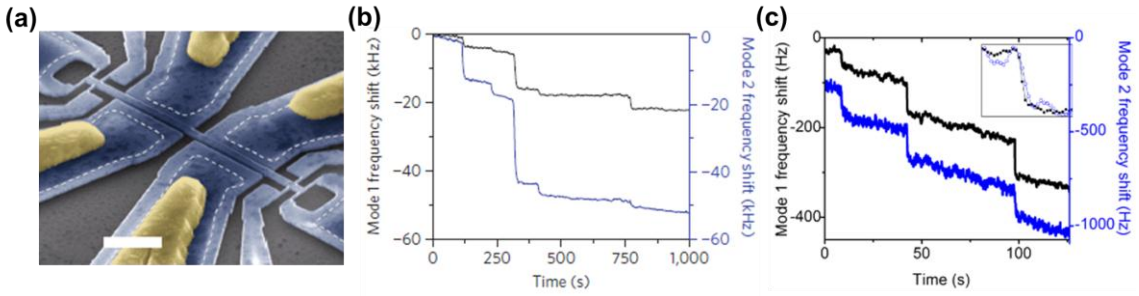

Fig. 1-3 NEMS-based mass detection in real time. (a) Electron micrograph of a representative device in the study. (b) Plots of frequency shift vs. time for the first and the second modes of the doubly-clamped resonator as individual gold nanoparticles and (c) human IgM land on the resonator from the ion source of ESI [21].

response times as shown in Fig. 1-3. In addition, there are still challenges for this technology because (1) this approach needs the cooling system for sample stages to operating temperature such as 70 K for the gold nanoparticle samples and 140 K for the IgM samples, specially to prevent captured ions from rapidly desorbing from the device's surface, (2) the resonance frequency drift caused by pressure variation and large environmental noise can lead to misreading of mass values determined, (3) the resonance frequency shift does not only depend on the mass of the molecule absorbed to the surface but also depends on where the molecule attaches along the surface, (4) a spectra of the same material with two different charge states can be distinguished with the different m/z in the traditional mass spectrometry using a mass analyzer (e.g. time-of-flight (TOF)), while NEMS based mass spectrometry is sensitive to only the given mass of the molecule, followed by producing the same mass spectra regardless of individual charge states, and finally (5) long lasting usage of the devices can cause malfunction in detecting molecules and difficulty in fitting from frequency shift to mass weight due to unstable resonant

frequency values by damaged devices and remnant piled up on the surfaces. Thus, NEMS-based mass spectrometry still has many obstacles needed to be solved for practical use.

Therefore, a new type of detector technology is required to have large active areas, mass independent response with high sensitivity and accuracy, fast response time, compatibility to existing technologies of mass spectrometry via using advantages of ESI or MALDI as an ion source and simple but powerful time-of-flight (TOF) as the mass analyzer. Moreover, the new type of detector should be suitable for practical use in the future and have long lasting access and durability of use. Based on those criteria, the new types of detectors presented in next sections will be coupled to MALDI-TOF mass spectrometry.

1.1.2 Principle of MALDI-TOF Mass Spectrometry (MS)

MALDI is the abbreviation for "Matrix-Assisted Laser Desorption/Ionization". The sample for MALDI is uniformly mixed in a large quantity of matrix. The schematic diagram of a MALDI-TOF mass spectrometry is illustrated in Fig. 1-3. The matrix absorbs the ultraviolet light from the laser converts it into thermal energy. A small part of the matrix heats up rapidly (nanoseconds) and is vaporized, together with the actual protein. Charged ions of various sizes are generated on the sample plate. A high DC voltage (HV) between the sample plate and ground attracts the ions into the direction of the detector (see Fig. 1-4). The velocity of the attracted ions is determined by the law of conservation of energy. As the high DC voltage applied is constant with respect to all ions,

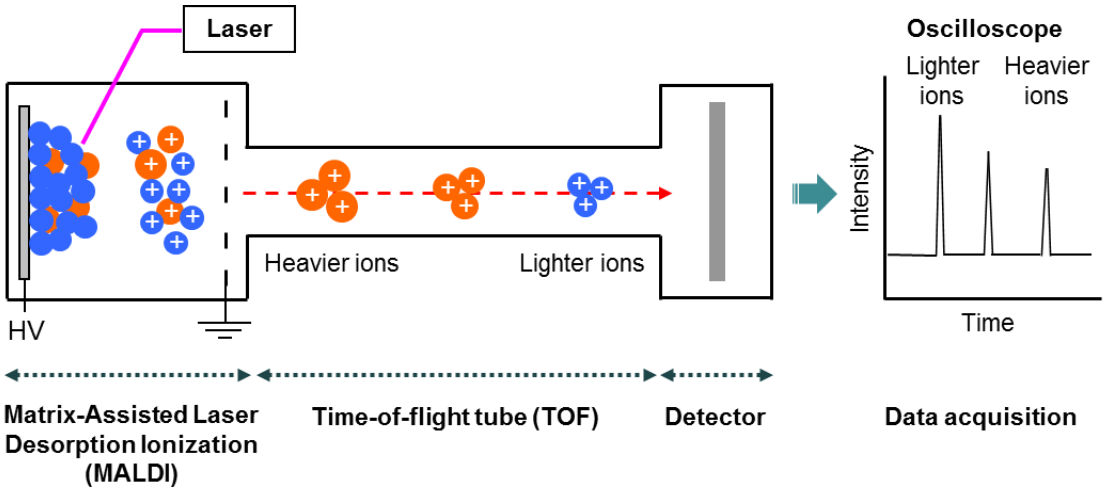

Fig. 1-4 Schematic diagram of a MALDI-TOF mass spectrometry. Ions are desorbed and ionized via energy transfer from the matrix to the proteins by laser irradiation. This step is followed by acceleration via the high DC voltage and flight through the tube. Lighter ions with higher velocities fly faster to the detector while heavier ions drift more slowly. The detector senses each ion arriving at a given time and the impact is recorded by the oscilloscope in real time.

ions with smaller *m/z* value (lighter ions) and more highly charged ions move faster through the time-of-flight tube (Electric field free region) until they reach the detector. Consequently, the time of ion flight differs according to *m/z* value of each ion. The potential energy of the charged ion in the electric field exerted by high DC voltage as it leaves the ion source must equal its kinetic energy.

$$PE = QV = zqV = KE = \frac{1}{2}mv^2 = \frac{1}{2}m\left(\frac{l}{t}\right) \tag{2.1}$$

where Q is total charge on the ion, V is the voltage difference in ion source, z is the number of charges on the ion, q is the elementary charge of 1.6×10^{-19} Coulomb, m is the mass of the ion, v is the drift velocity of the ion, t is the drift time of the ion, and l is the total drift distance.

Therefore, the drift time is proportional to the square root of the mass as defined by

$$t = l\sqrt{\frac{m}{2zqV}}\,. \tag{2.2}$$

Once the output signal is recorded in real time by the oscilloscope, the mass spectra is collected by obtaining *m/z* values. The relation between *m/z* and the drift time is described by

$$\frac{m}{z} = t^2\frac{2qV}{l^2}\,. \tag{2.3}$$

1.2 Application of nanomembrane detectors in MALDI-TOF MS

In order to overcome the limitation of current detectors in MS discussed previous sections, several approaches have recently been pursued by Park *et al*. [24-26]. The possibility of using nanomembranes for protein MS has been demonstrated for Silicon nitride (Si_3N_4) and Silicon as materials for nanomembranes. The MS method of choice for this approach is MALDI-TOF.

1.2.1 Silicon nitride (Si_3N_4) nanomembrane

The new principle is introduced for ion detection in TOF MS in which an impinging ion packet excites mechanical vibration in a silicon nitride (Si_3N_4) nanomembrane [24, 25]. As shown in Fig. 1-5, the nanomembrane detector consists of four parts, a nanomembrane, an extraction gate, a microchannel plate, and an anode. It is

placed at the end of the flight tube in a commercial MALD-TOF mass spectrometer (Perseptive Bisosytems Voyager-DE STR). The square (5 mm×5 mm) nanomembrane consists of a suspended trilayer of Al/Si_3N_4/Al. The Al metal layer on top acts as a cathode for electron emission and the bottom Al layer forms the absorber of the incident ions.

In the absence of ion bombardment, the nanomembrane is stationary, but it emits electrons by field emission and is bulged toward the extraction gate due to the applied electric field. Since the intensity of field emission is strongly dependent on the electric field generated between the nanomembrane and the extraction gate electrode, mechanical vibrations of the nanomembrane excited by ion bombardment translate into corresponding oscillation in the field emission current as shown in Fig. 1-5.

The field emission current is superimposed on the DC field emission current, which is then amplified by the microchannel plate (MCP) and collected by the anode. The kinetic energy of the proteins delivered by the initial high DC voltage of the ion source is transformed into thermal energy during impact. This raises the temperature in the vicinity of the impact site causing a nonuniform temperature distribution across the nanomembranes. This thermal gradient leads to thermomechanical forces which exert nanomembrane mechanical vibrations. Fig. 1-5 (d) shows a MALDI mass spectrum obtained using the Si_3N_4 nanomembrane detector for an equimolar protein mixture (3.3 μM) of Insulin (5,729 Da), bovine protein mixture (66,429 Da), and immunoglobulin G (IgG, ~150,000 Da) without large loss of sensitivity at higher masses.

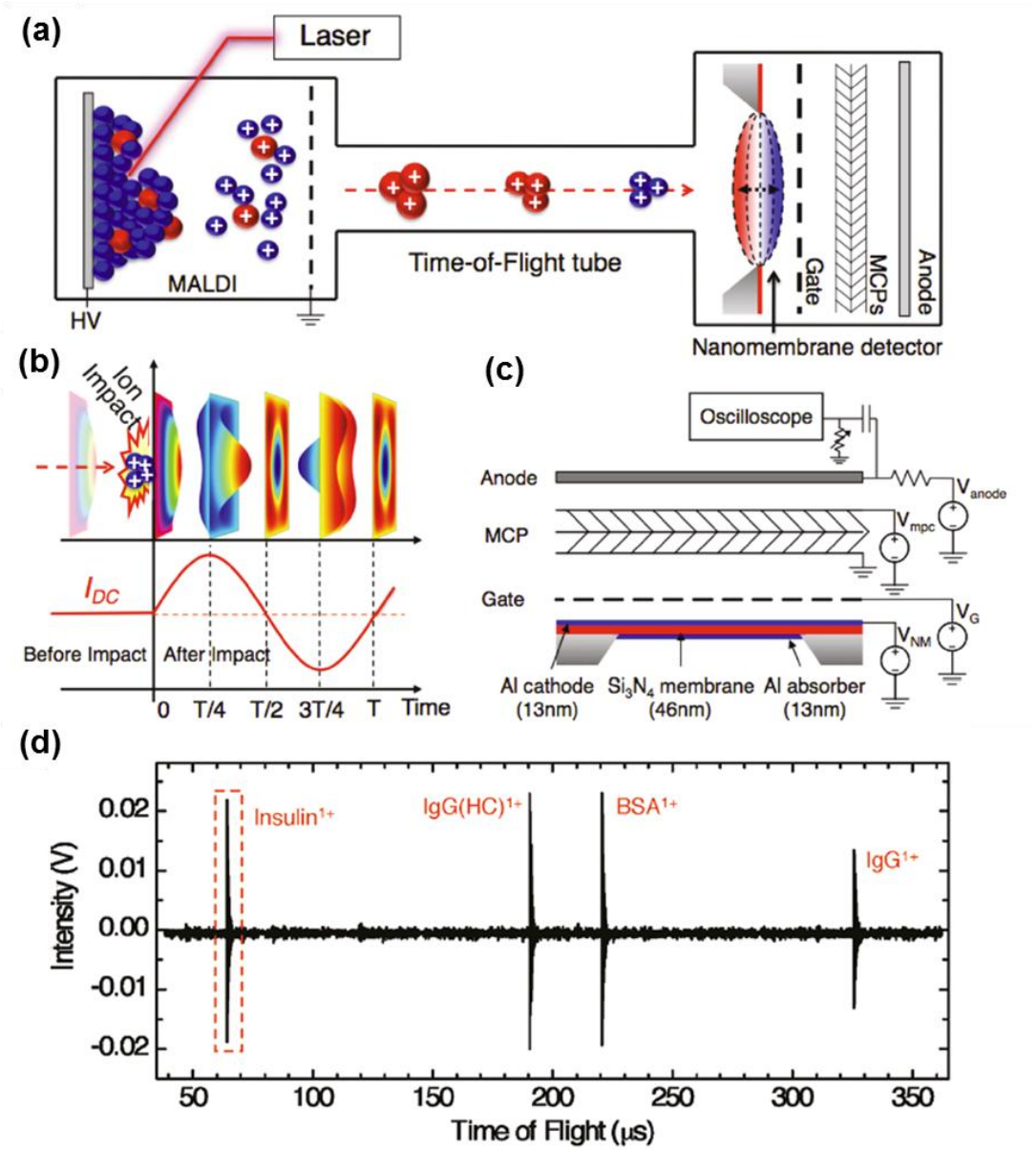

Fig. 1-5 Operation of a Si_3N_4 nanomembrane detector. (a) Schematic of the detector coupled to a MALDI-TOF mass spectrometer. (b) Detailed illustration of the operation principle of the detector. Ion bombardment excites mechanical vibrations of the nanomembrane, resulting in a modulation of the field emission current. (c) Schematic of the detector configuration, consisting of a trilayer made of Al/Si_3N_4/Al, an extraction gate, MCP, and an anode. (d) Mass spectrum detected for an equimolar protein mixture of Insulin, BSA, and IgG [24, 25].

However, the factor that detection depends on vibration of nanomembranes at a

given moment can give the challenge to long lasting use since the damage on mechanical structure of membranes via continuous vibration and impacting the surface by ions and remnants of ions on the surface can cause the degrading of the quality factor, larger response time and the fundamental frequency changes in vibration which affect the sensitivity in detection of ions. Moreover, the oxidization of Al cathode and absorber during handling the device in air can cause performance degradation on electron field emission from the Al layer.

1.2.2 Silicon nanomembrane

The demand for enhancing performance and durability, which is stemmed from Si_3N_4 nanomembrane in previous application to MS as a detector, results in new application with silicon nanomembrane [26]. This type of detector uses phonon-assisted field emission in silicon nanomembranes via phonon transfer by heat generated from kinetic energy at the moment of ion impact. Impinging ion packets on one side of the suspended silicon nanomembrane generate nonequilibrium phonons, which propagate quasi-diffusively and deliver thermal energy to electrons within the silicon nanomembrane as shown in Fig. 1-6. These nonequilibrium phonons deliver sufficient thermal energy to the electrons within the nanomembrane and excite them to higher energy states, thereby allowing them to overcome the vacuum barrier and escape from the nanomembrane surface via field emission (so called ‘phonon-assisted field emission’) as shown in Fig. 1-6 (c). This mechanism enhances electron emission from the surface

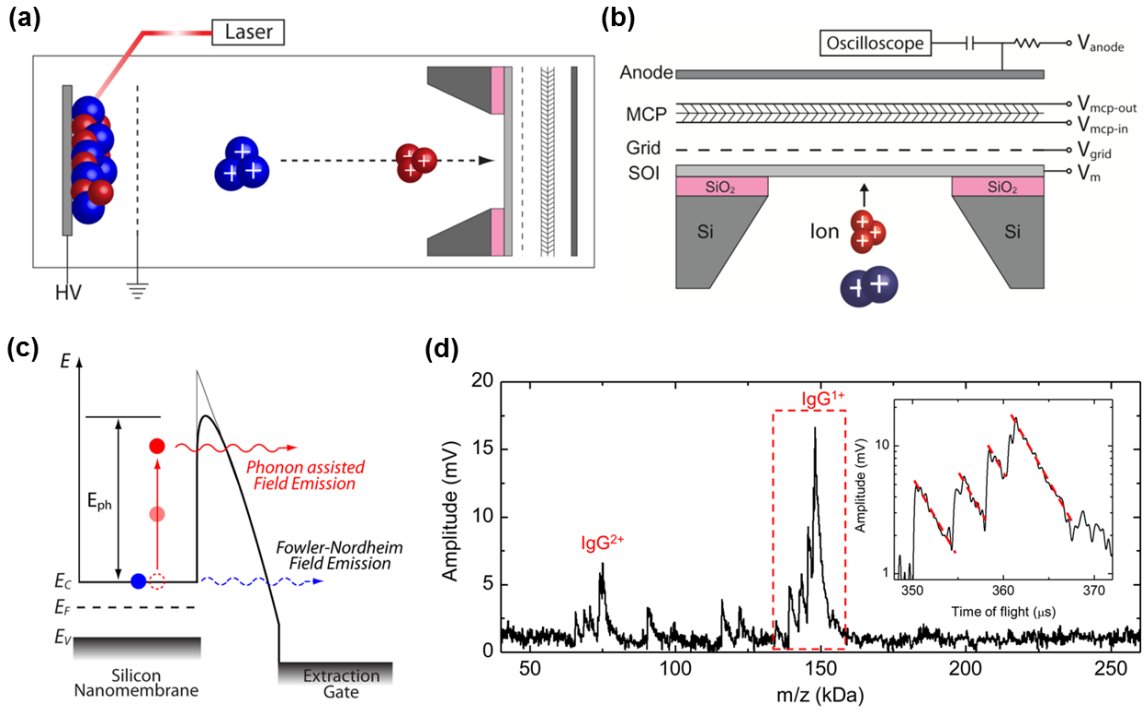

Fig. 1-6 Operation principle of the silicon nanomembrane detector. (a) Schematic of the detector coupled to a MALDI-TOF mass spectrometer. (b) Schematic representation of the detector, consisting of a 180nm thin silicon nanomembrane, an extraction gate, MCPs, and an anode. (c) Energy band diagram showing phonon-assisted field emission. (d) Mass spectrum for IgG obtained using the silicon nanomembrane detector [26].

with an electric field applied to it. In terms of response times, the phonons travel much faster in out-of-plane (in thin thickness direction comparable to mean free path of the phonon) than via normal diffusion but slower than in pure ballistic transport. This leads to a sharp onset with a rise time of 350 ns in the mass spectrum in time-of -flight axis shown in an inset of Fig. 1-6 (d). The exponential decay with a decay constant of 3 μs followed by the sharp onset mainly stems from the much slower process of the in-plane heat diffusion (in much larger lateral dimension than mean free path of the phonon). The nonequilibrium phonon-assisted field emission in the suspended nanomembrane

connected to an effective cooling of the nanomembrane via field emission allows mass analysis of MegaDalton ions such as IgM (~1 MDa) with high mass resolution at room temperature. Moreover, this type of detector also operates at acceleration voltages of only 9 kV for the protein masses up to 39,212 Da (Aldolase) which enables possible application of the detector to other types of MS systems such as ESI-TOF. The detector of Silicon nanomembrane demonstrates the exceptional mass range and sensitivity for ultrahigh protein masses with 200 times smaller area than that of a typical MCP detector with a 1 in. diameter.

However, several challenges still remain for the silicon nanomembrane detectors. Since the detector uses pure silicon as a base material, oxidization of the membrane during handling can cause weakening of the output signal, which in turn affects performance of the device. The resolution of the detector can be improved further by enhancing heat diffusion by applying materials with a larger thermal conductivity (e.g. diamond) instead of silicon. The durability can also be improved by applying harder materials such as diamond.

1.3 Diamond as a material for the detector

Diamond possesses outstanding properties so that its exploitation in many fields is desired and sought for several years now. It becomes gradually more interesting material for its exceptional physical, electrical and mechanical properties such as high thermal conductivity, chemical inertness, optical transparency, negative or small positive electron affinity, high mechanical stability, corrosion resistance, and so on. Although

Table 1-1 Material properties of Silicon, Diamond, and Germanium [27-29]

Property	Silicon	Diamond	Germanium
Thermal conductivity (W/mK) (at 300K)	149	2320	60.2
Phonon mean free path (nm)	40 ~ 300	100 ~ 460	30 ~ 480
Young's modulus (GPa)	130	1200	103
Fracture strength (MPa)	1000	5300	90
Melting point (K)	1687	3823	1211

diamond has a crystal structure identical to its more common relatives silicon and germanium, its properties differs from the others as shown in Table 1-1. Based on the overall properties of diamond, use of diamond as a material for nanomembrane detectors has theoretically a high potential. High thermal conductivity and long phonon mean free path can make the phonon propagation through nanomembranes more efficient and cooling of nanomembranes more effective, followed by improved performance. Moreover, the high Young's modulus of diamond offers long lasting durability even in harsh environment. In addition, the surface of diamond is relatively inert to chemisorption, which means that the diamond nanomembrane detector has a high chemical stability.

Based on the views of the existing challenges from Si_3N_4 and silicon nanomembranes discussed in previous sections, diamond material owing to its

theoretically exceptional properties such as extreme hardness, chemical inertness, high thermal conductivity, and long phonon mean free path can be one of promising candidates for application to the nanomembrane detector in MS. Although thermal conductivity and phonon mean free path are degraded from single crystal or natural diamond (not easily obtainable in reality) shown in Table 1-1 to polycrystalline diamond due to grain size effects [30], the outstanding properties of diamond itself are still attractive to approach as a diamond nanomembrane detector for proteomics.

Chapter 2

Large-area freestanding Diamond nanomembranes

As discussed in the previous chapter, application of nanomembranes as detectors in MALDI-TOF MS offers improved sensitivity for high mass detection. Diamond as a material for these nanomembrane detectors can be one of the promising candidates owing to exceptional electrical, physical, and mechanical properties. Single crystal diamond may be the best material for detector applications in proteomics. In reality, those types of diamond materials are not obtainable easily (e.g. very expensive price or rare to get). The polycrystalline chemical vapor deposition (CVD) diamond can be another type of diamonds easily assessable in real world although some of properties are degrading from natural diamond according to the grain sizes, direction, thickness of layer, and so on. However, the economical access to materials can be one of important factors in extended application in spite of the degrading effects of properties. One of types of polycrystalline CVD diamonds popularly used in many applications [31, 32] is ultra-nanocrystalline diamond (UNCD) developed by Argonne national laboratory (*Argonne, IL*) in the early 1990s, followed by commercializing. Nowadays, the wafers with various types of UNCD on different substrates are sold by the company (*Advanced Diamond Technologies, Inc., Romeoville, IL*) with easy access to get.

Therefore, the diamond nanomembrane detectors for application in mass spectrometry are demonstrated based on UNCD as the type of diamond materials in this study.

2.1 Boron doped (*p*-type) Ultra-nanocrystalline diamond (UNCD)

Ultra-nanocrystalline diamond (UNCD) is deposited on various types of wafer substrates with the method of hot filament chemical vapor deposition (HFCVD) (*Advanced Diamond Technologies, Inc., Romeoville, IL*). In this deposition method, the process gas (usually mixture of 1% CH_4/H_2) is fed into the reactor chamber where it is activated by a coil metallic filament maintained at high temperatures. Diamond is deposited onto the surface of the wafer via a gas-phase chemical reaction [33]. The trimethylboron (TMB), $B(CH_3)_3$ gas is fed into the reactor chamber together with mixture of CH_4 and H_2 as a boron dopant in the case for boron doping of diamond [34]. In view of fabrication prices, the HFCVD technique has the advantage of uniform deposition of polycrystalline diamond over large area wafers at low cost.

2.2 Fabrication

The fabrication of freestanding diamond nanomembranes is depicted in Fig. 2-1: the processes begin with boron doped (*p*-type) diamond-on-insulator (DOI) wafer substrates containing ultra-nanocrystalline diamond (UNCD) layers of a 100 nm and a 200nm thickness, respectively (*Advanced Diamond Technologies, Inc., Romeoville, IL*).

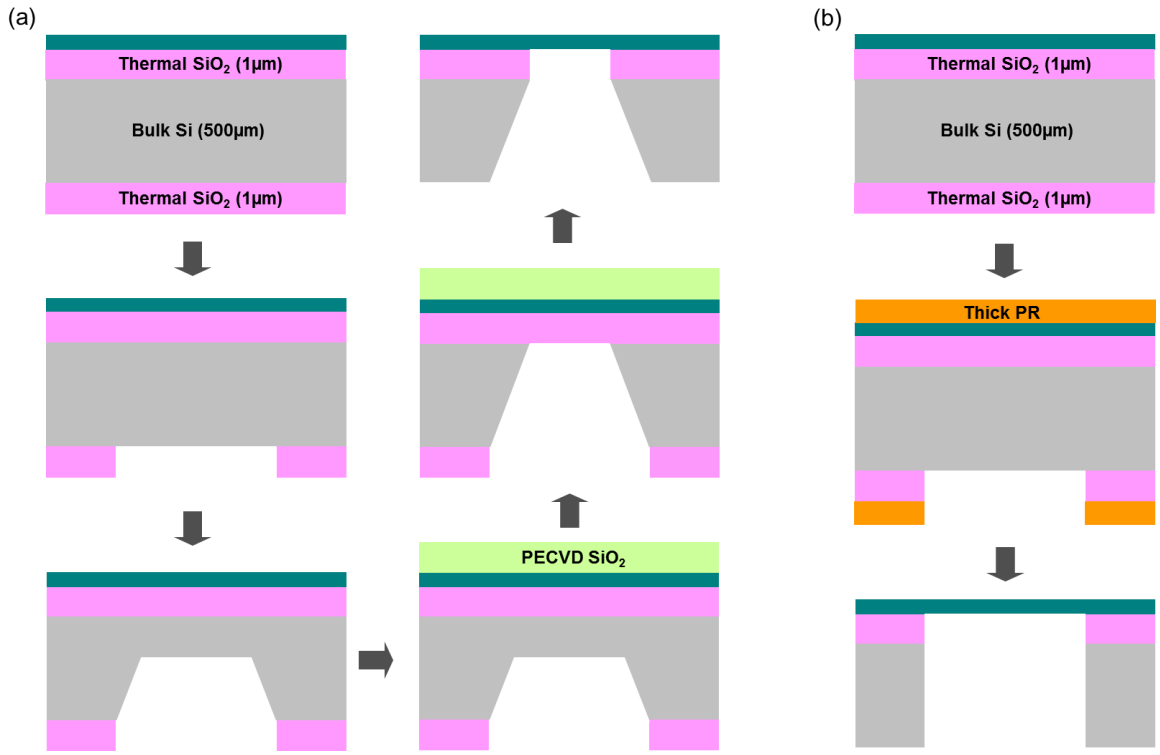

Fig. 2-1 Sequence of the two fabrication procedures for freestanding diamond nanomembranes applied in this thesis: using (a) wet etching of bulk Si for generating square membranes and (b) by dry-etching of bulk Si for circular membranes or other desired shapes (see text for details).

We have employed two different types of fabrication processes, i.e. (a) wet etching based on tetra-methyl-ammonium hydroxide (TMAH) solution and (b) dry etching with the Surface Technology System (STS) Multiplex Inductively Coupled Plasma (ICP) for square membranes, circular membranes, or any other shapes. For both cases, the fully suspended diamond nanomembranes can be realized by etching the substrate layers through windows of defined shapes on the backsides of the samples.

Typically, we apply 1 µm thick thermal SiO_2 layers as an etch mask for the anisotropic wet etch step (see Fig. 1-1 (a)) of a 500µm-thick bulk silicon layer using

TMAH solution [35, 36]. These layers are then patterned with square windows defined by optical lithography and then the SiO_2 is etched in a buffered oxide etch (BOE). In order to protect the diamond layer during wet etching, a SiO_2 layer is deposited on top of it via plasma-enhanced chemical vapor deposition (PECVD). This ensures protection of the suspended structure from physical damage during the release from the silicon substrate. This 3 µm-thick PECVD SiO_2 layer is deposited after about 60% of the silicon substrate is etched by considering the much lower etch selectivity of silicon to PECVD SiO_2 than thermal SiO_2 [37]. Finally, the freestanding diamond nanomembranes are obtained by totally etching away the bulk silicon substrate within the square window, followed by removing both layers of SiO_2 in BOE solution. Fig. 2-2 (a) shows an optical microscope image of a $400 \times 400\ \mu m^2$ freestanding 100 nm-thin diamond nanomembrane.

The freestanding circular membranes in Fig. 2-2 (b) are realized via dry-etching of the silicon substrate using the STS Multiplex ICP. The circular window patterns of the thermal SiO_2 layer are defined by optical lithography, hence any kind of shape can be defined. This is of importance for engineering the mechanical stress. Afterwards a BOE-step is employed as before. Since the 1µm-thin thermal SiO_2 layer is insufficient as an etch-mask to resist several hours of dry etching the silicon [38, 39], we deposit a thick photoresist (PR) layer. The PR is coated with a thickness of around 30 µm on the surface of the diamond layer, i.e. we repeat spin coating of 10 µm three times. This ensures protection of the diamond layer from physical and electrical damage [40, 41] by the O_2-plasma. This PR coating is apparently repeated after every hour of dry-etching in order to retain a safe thickness. Once the bulk silicon substrate within the circular window is

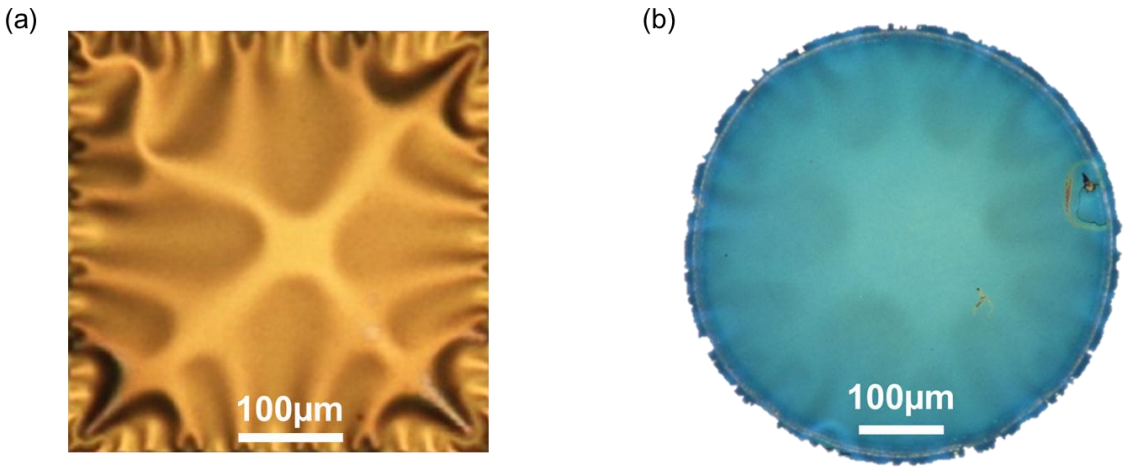

Fig. 2-2 Freestanding diamond nanomembranes: optical microscope image of (a) the 400×400 μm^2 free-standing 100 nm-thin diamond nanomembrane and (b) the 500μm diameter-freestanding 200nm-thin diamond nanomembrane. The specific buckling patterns are generated after release of the membranes.

completely etched out, the freestanding circular diamond nanomembrane is finally obtained by stripping the remaining PR with acetone, followed by removing both layers of SiO_2 in a BOE solution. Fig. 2-2 (b) shows the final optical microscope image of a 500 μm diameter-freestanding 200 nm-thin diamond nanomembrane.

As shown in Fig. 2-2, the free-standing nanomembranes reveal buckling patterns formed during releasing the structure from the substrate. The releasing procedure of the diamond membrane from the supporting stack of layers causes the simultaneous release of the residual stress built up inside the membrane. This embedded stress is internalized through the chemical vapor deposition (CVD) process during diamond deposition on SiO_2/Si. In its entirety the buckling patterns depend on the total stress distribution, given by the embedded stress and the compressive residual stress depending on the geometry formed [42-45].

2.3 Stress analysis

The deposited thin film layers can contain residual stress arising due to the mismatch of the thermal expansion coefficients, non-uniform plastic deformation, lattice mismatch, substitutional or interstitial impurities, and the growth processes in general [46, 47]. In our case, the thin diamond layer can have the residual stress built up during the CVD definition of the diamond on the SiO_2/Si substrate and other steps in the fabrication process. This residual stress is released during the processes of releasing the diamond membranes. This in turn leads to buckling patterns of the membranes [42-45]. The buckling profiles of the membranes are investigated in the optical profilometer (*Zygo NewView 6300 white light interferometer, Zygo Corp., Middlefield, CT*). Fig. 2-3 shows the buckling profiles measured on the front sides (etching is always performed from the back side) of the samples for a (*i*) 485×485 μm^2 membrane (Fig. 2-3 (a)), the (*ii*) 270×270 μm^2 membrane (Fig. 2-3 (b)), and a (*iii*) 500µm diameter-circular membrane (Fig. 2-3 (c)). The maximum out-of-plane displacement referenced to the outer area of the membrane is 10.1 µm, 5.7 µm, and -6 µm (downward) for (*i*), (*ii*), and (*iii*), respectively.

The relationship between the pressure forced to the membrane and the displacement is given by [48, 49] and can be noted for square membranes as

$$P(\zeta_{\max}) = 13.6\frac{t_M \zeta_{\max}}{a_M^{\,2}}\left(\sigma + 1.61\frac{\zeta_{\max}^{\,2}}{a_M^{\,2}}\frac{(1.446-0.427\nu_M)E_M}{1-\nu_M}\right) \qquad (2.1)$$

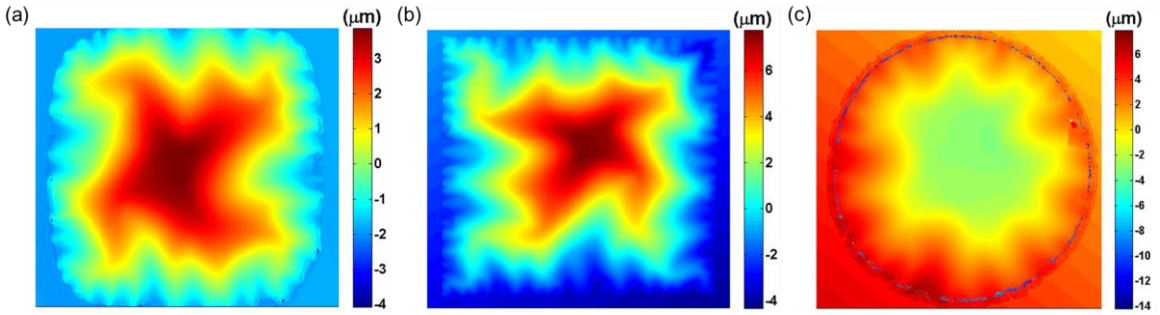

Fig. 2-3 Color-scale profiles of the bulging patterns for three different diamond membranes. The profiles indicate the relative displacement due to the embedded stress. Shown are (a) 485×485 μm^2 and (b) 270×270 μm^2 diamond membranes with 100nm thickness bulging upwards, while in (c) circular 500μm diameter membrane of 200nm thickness is buckling downwards.

While for circular membranes we have

$$P(\zeta_{\max}) = 4\frac{t_M \zeta_{\max}}{R_M^{\,2}}\left(\sigma + \frac{2}{3}\frac{\zeta_{\max}^{\,2}}{R_M^{\,2}}\frac{E_M}{1.026 - 0.793\nu_M - 0.233\nu_M^{\,2}}\right) \tag{2.2}$$

where P is the applied pressure, $\zeta_{\max}$ is the displacement at the center of the membrane, a_M is the half-edge length of the square membrane, R_M is the radius of the circular membrane, t_M is the thickness of the membrane, E_M is the Young's Modulus, ν_M is the Poisson's ratio, σ is the residual stress.

The displacement at the center of the freestanding membrane due to buckling by only residual stress can hence be approximately obtained by assuming the pressure P to be zero in Eqs. (2.1) and (2.2). The terms inside the parentheses on the right consequently should be zero to obtain meaningful results. Then, we can reversely estimate the values of σ based on $\zeta_{\max}$ measured by the optical profilometer. The residual stress built up in the membranes is then estimated to be (-840 ± 20) MPa (compressive) and (-340 ± 40)

MPa (compressive) for square membranes with 100 nm thickness and for circular membranes with 200 nm thickness, respectively. The membranes show buckling upwards and downwards, as shown in Fig. 2-3. We find both bulging up and down with displacements of ± 5.7 μm in case of the 270×270 μm^2 membranes with 100 nm thicknesses with bistable states. Since the second term within the parentheses of both Eqs. (2.1) and (2.2) has a square dependence on ζ_{max}, the compressive residual stress can lead to a positive or negative deflection, i.e. it is bistable [48, 50].

Chapter 3

Electrical and mechanical characteristics of Diamond membranes

The investigation of electrical and mechanical characteristics of diamond nanomembranes are very interesting in terms of the freestanding large-area thin structure itself and also necessary for operation in mass spectrometry application, which is affected by mixed characteristics of the structures in the performance of the nanomembrane detector. Mechanical displacement and electron field emission characteristics of diamond nanomembranes play important roles regarding ion detection.

3.1 Electron field emission measurement at room temperature

In order to validate the applicability of the doped freestanding diamond nanomembranes as field emitters, we performed a set of measurement in our home-made MALDI-TOF unit (~2.0×10^{-7} mbar) as shown in Fig. 3-1 (a). The schematic diagram of the experimental configuration is shown in the inset of Fig. 3-1 (b): the electric field is ramped between the diamond nanomembrane and the extraction gate by applying voltages to the membrane (V_{DM}) and the extraction gate (V_G). This reduces the energy barrier for electrons inside the diamond membrane, so that they can tunnel out.

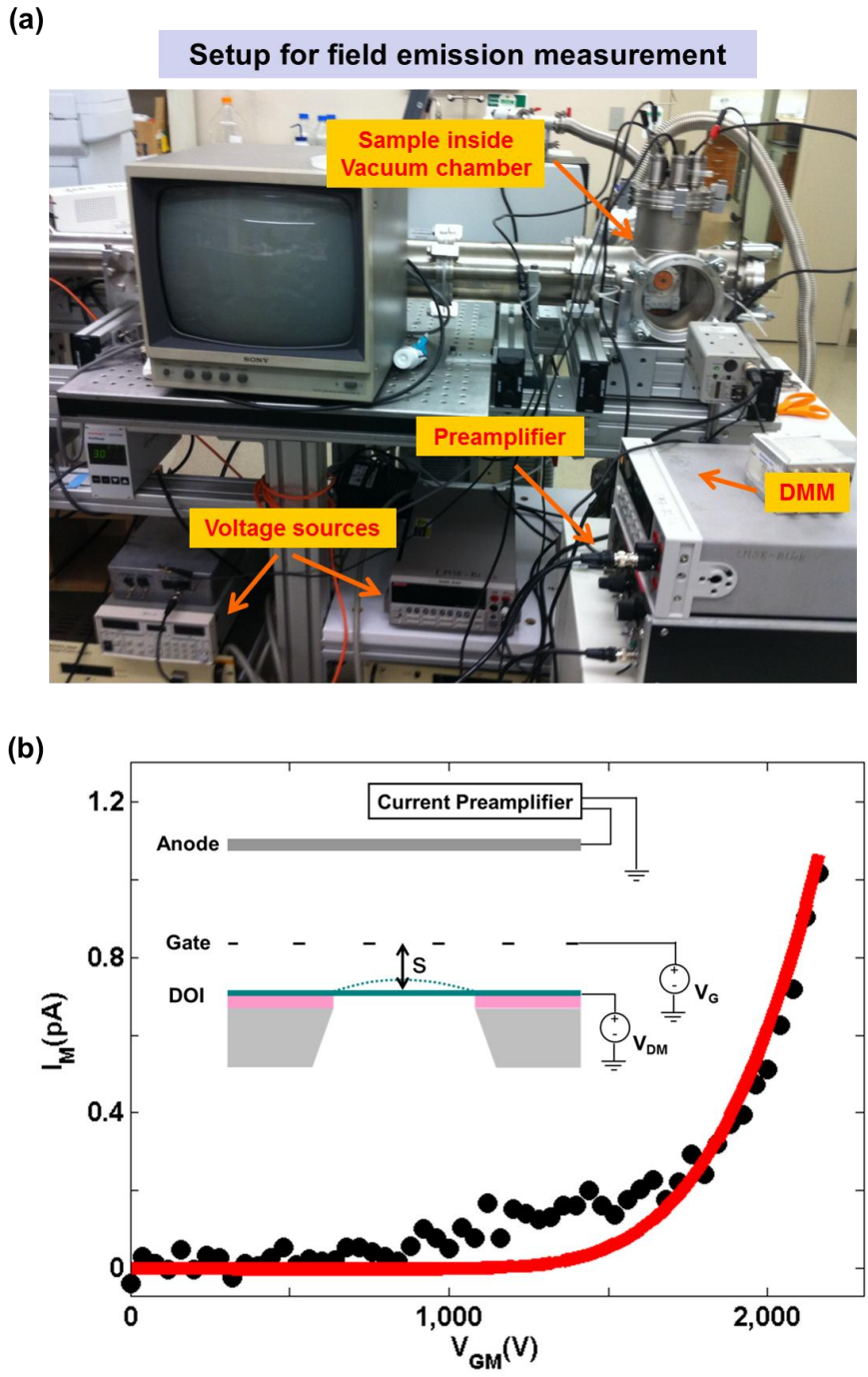

Fig. 3-1 Measurement of field emission from the freestanding diamond nanomembrane at room temperature. (a) Setup for field emission measurement in our home-made MALDI-TOF unit. (b) *IV*-curves of the measurement are given by the black filled circles, while the theoretical fit is given by the red line. Inset: schematic diagram of the experimental configuration.

The extraction grid funnels the electrons finally to the anode [24]. In Fig. 3-1 (b) the *IV*-characteristic of the 100 nm thin nanomembrane is given by black filled circles as a function of the voltage applied between the diamond membrane and extraction gate, V_{GM}. In order to model the electron field emission analytically in this particular system, the mechanical and electrical behavior of the freestanding diamond nanomembrane has to be considered [24]. Effectively, the nanomembrane deforms due to the electromechanical pressure exerted by applying V_{GM}. Hence, the electric field strength between the membrane and the extraction gate is altered.

3.2 Theoretical approach to electron field emission

In the freestanding membrane structure, electron field emission is affected by the mechanical and electrical properties of the structure which differs from that of original films deposited on the bulk surface. The applied voltage between the membrane and extraction gate causes the displacement of the membrane and changes the electrical field again and vice versa. The field emission from the membrane at a given moment also depends on the electric field strength. In order to approach electron field emission from freestanding diamond nanomembranes theoretically, all these effects have to be considered for modeling.

3.2.1 Modeling of displacement under the electrostatic force

We can describe this electromechanical circuit by considering the total electric potential energy stored between the nanomembrane and the extraction grid, which is

defined by

$$W = \frac{1}{2} C V_{GM}{}^2 . \tag{3.1}$$

The capacitance between the nanomembrane and the extraction grid gate can be estimated by [24, 51]

$$C = \frac{2\pi\varepsilon_0 lN}{\ln\frac{2s}{r}}, \tag{3.2}$$

where ε_0 is the permittivity, l is the side length in the edge of the membrane, N and r are the number and the radius of metal wires in mesh, which is acting as the extraction gate over the membrane, respectively, and s is the distance between the membrane and the extraction gate as shown in the inset of Fig. 3-1 (b).

Therefore, the pressure exerted to the membrane due to the electrostatic force can be obtained by using Eqs. (3.1) and (3.2) following [24] to be

$$P_e = \frac{F_e}{A} = -\frac{\nabla W}{A} = \frac{2\pi\varepsilon_0 lN}{As\left(\ln\frac{2s}{r}\right)^2} V_{GM}{}^2, \tag{3.3}$$

where A is the area.

In our case, the pressure obtained from Eq. (3.3) at a given V_{GM} is used on the left side of Eq. (2.1) for calculating $\zeta_{\max}$ at V_{GM}.

The shape of the deformed diamond nanomembrane as a function of position, $\zeta(x, y, V_{GM})$ is described according to the maximum displacement at V_{GM} with the following relationship [24, 49] to yield

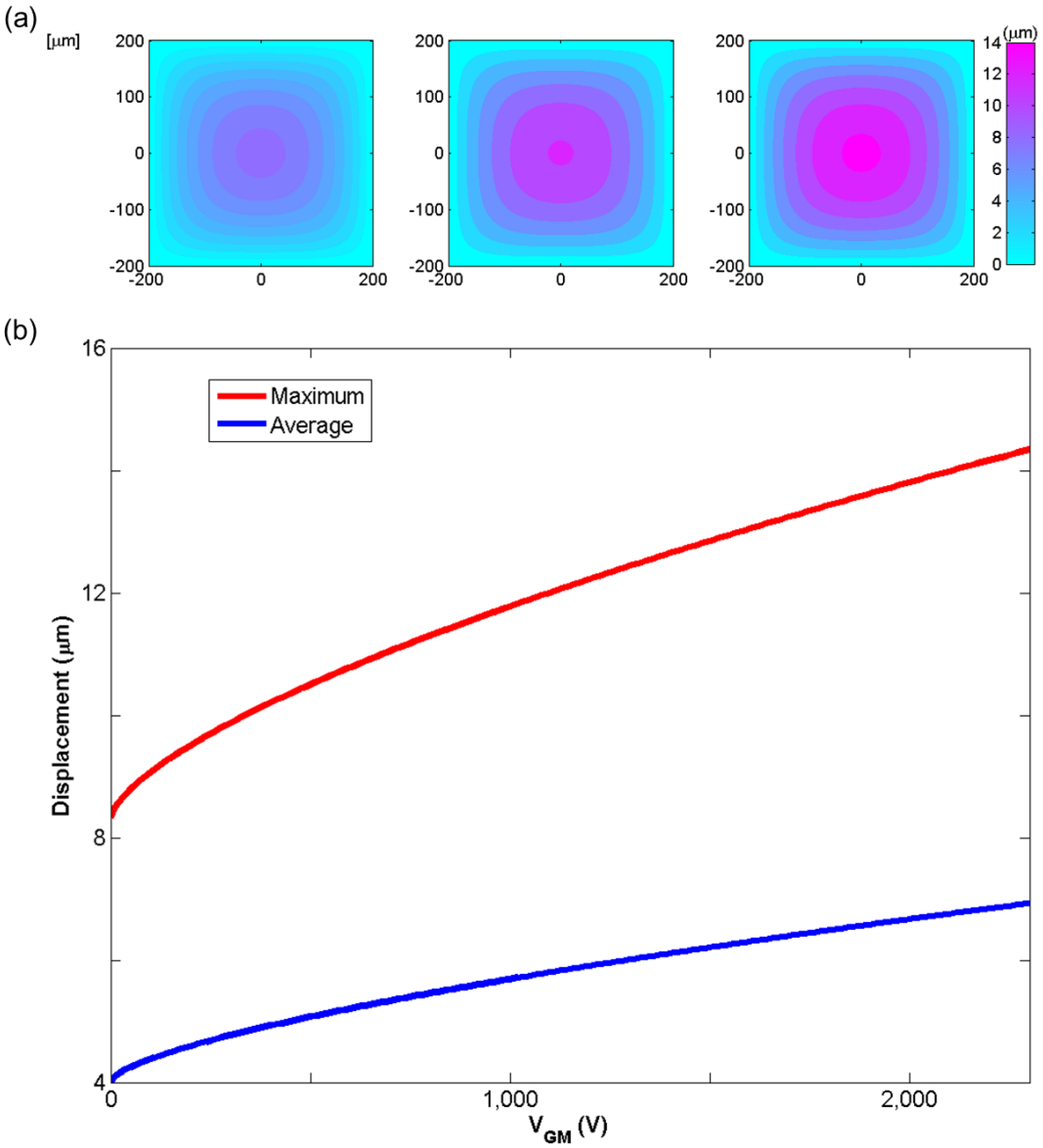

Fig. 3-2 Theoretical modeling of the displacement on the membrane: (a) Estimated displacement profile through the membrane at the applied voltages such as 0 V, 1,150 V and 2,300 V of V_{GM} and (b) estimated maximum (red line) and average (blue line) displacement over the membrane's surface as a function of applied voltage, V_{GM}.

$$\zeta(x,y,V_{GM}) = \zeta_{\max}(V_{GM})\left(1+0.401\frac{x^2+y^2}{{a_M}^2}+1.12\frac{x^2y^2}{{a_M}^4}\right)\cos\frac{\pi x}{2a_M}\cos\frac{\pi y}{2a_M} \tag{3.4}$$

where a_M is one half of the membrane's edge length. The coefficients, 0.401 and 1.12 are the values obtained with the Poisson's ratio ν_M [15].

The displacement profiles of the diamond nanomembrane under applied voltages of V_{GM} can be found by using Eqs. (2.1), (3.3), and (3.4) based on the residual stress obtained from measured initial buckling (shown in Fig. 2-3) of the membranes. Fig. 3-2 (a) shows the estimated displacement profile through the membrane, $\zeta(x,y,V_{GM})$ at the applied voltages such as 0 V, 1,150 V, and 2,300 V of V_{GM} as the examples among whole range of voltages applied. The average displacement (ζ_{ave}) over the membrane's surface at a given V_{GM} can be obtained by [24]

$$\zeta_{ave}(V_{GM}) = \frac{\int_{-a_M}^{a_M}\int_{-a_M}^{a_M}\zeta(x,y,V_{GM})dxdy}{(2a_M)^2} = 0.48314\,\zeta_{\max}(V_{GM}) \tag{3.5}$$

Therefore, the average distance $s(V_{GM})$ between the membrane and the extraction gate can be found by

$$s(V_{GM}) = s_0 - \zeta_{ave}(V_{GM}) = s_0 - 0.48314\,\zeta_{\max}(V_{GM}) \tag{3.6}$$

where s_0 is the initial average distance without applying V_{GM}.

The estimated maximum ($\zeta_{\max}(V_{GM})$) and average displacement ($\zeta_{ave}(V_{GM})$) over the membrane surface as a function of applied voltage, V_{GM} is shown in Fig. 3-2 (b) with the red line and blue line, respectively.

3.2.2 Theory of field emission from semiconductor materials

The Fowler-Nordheim (FN) equation [52] has been used to analyze field emission from diamond surfaces [53-55]. C. –L. Chen *et al.* [56] developed a modified theoretical model for field emission from p-type diamond surfaces (wide band gap semiconductor) based on the theory of field emission from semiconductor derived by R. Stratton [57, 58]. By using the theoretical model [56], S. –Y. Chen *et al.* [59] performed experimental work regarding the temperature dependence of field emission for boron-doped (*p*-type) diamond films.

The total field emission current density from freestanding diamond (boron doped, p-type) nanomembranes in our case can be modeled by [56, 59]

$$J = J_c + J_v = k_1 T^2 e^{-\frac{\theta}{kT}} e^{-k_2 \frac{\chi^{\frac{3}{2}}}{F}} + k_3 \frac{F^2}{\chi + E_g} e^{-k_4 \frac{(\chi + E_g)^{\frac{3}{2}}}{F}}. \tag{3.7}$$

Where J_c and J_v are the emission current densities from the conduction band and the valence band, respectively, χ is the electron affinity, E_g is the energy gap, and θ is the energy difference between the surface conduction band minimum and the Fermi level,

$$k_1 = \frac{qmk^2}{2\pi^2\hbar^3},\ k_2 = \frac{4\sqrt{2m}}{3q\hbar} v(y),\ k_3 = \frac{q^3}{16\pi^2\hbar^2 t^2(y)},\ F = \beta \frac{V_{GM}}{s(V_{GM})}. \tag{3.8}$$

Where $v(y)$ is a tabulated function involving an elliptic integral, $t(y)$ is another tabulated function closely related to $v(y)$ [60], and $s(V_{GM})$ is obtained from Eq. (3.6).

3.2.3 Theoretical fit to the measurement curve

The total emission current from the freestanding diamond nanomembrane is proportional to the effective area of the surface as given by

$$I = A_{eff} \times J \tag{3.9}$$

The analytical plot of the total emission current from the 400 µm×400 µm freestanding 100 nm-thin diamond nanomembrane is depicted as a red line in Fig. 3-1 (b). The curve is in good agreement with the results of the measurement. For explaining the discrepancy in the intermediate voltage range, more field emission mechanisms have to be considered.

3.2.4 Compensation of theoretical fits with electron emission mechanisms in three distinct field regions

Electron emission in the intermediate voltage range can be modeled as a combination of three emission mechanisms including thermionic emission, Schottky emission, and FN tunneling, which is based on natural logarithmic analysis of the measured current density as shown in Fig. 3-3 (a).

Thermionic emission [73] is acting primarily in the range of very small electric fields and consists of electrons being thermally excited with sufficient energy to overcome the energy barrier at the surface and thus being emitted into vacuum.

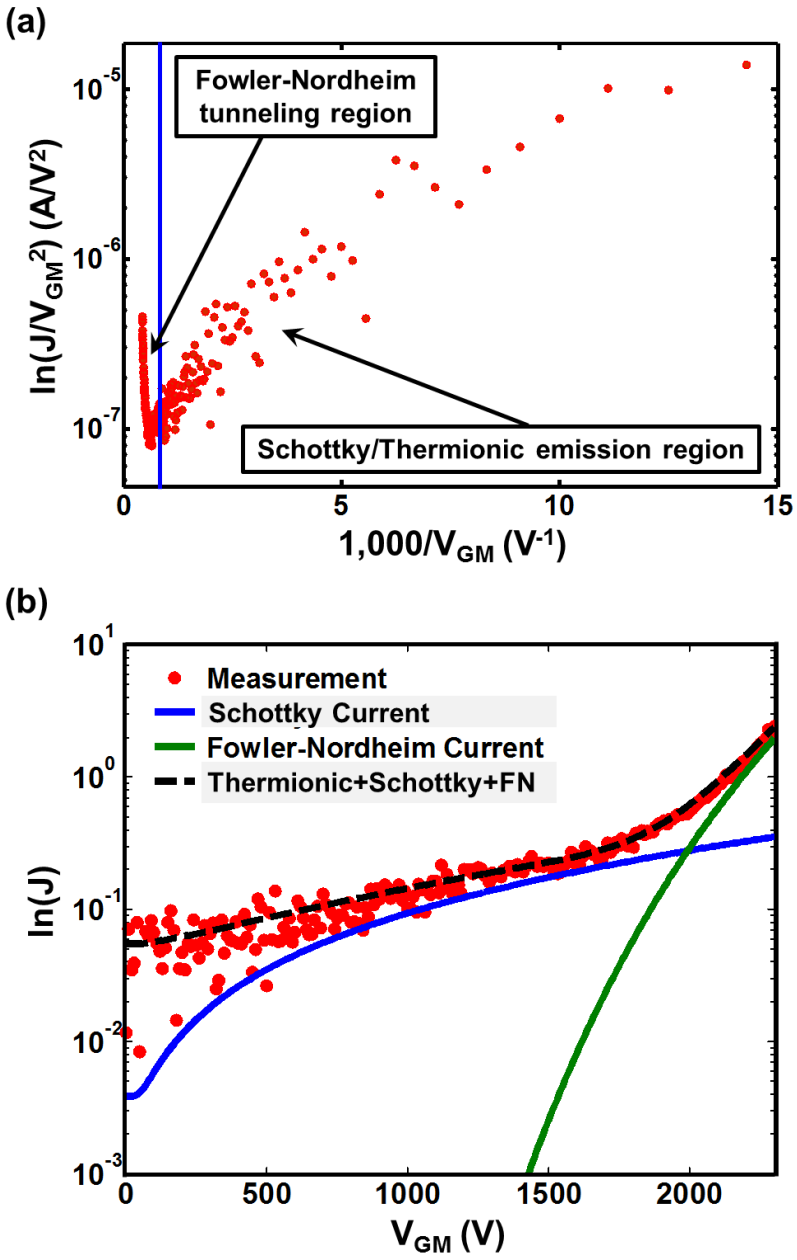

Fig. 3-3 Analysis of field emission via three distinct electron emission mechanisms. (a) Natural logarithmic plot of J/V_{GM}^2 vs. V_{GM}^{-1}. Measured field emission data (red filled circles) shows contribution of three distinct emission mechanisms. The linear region (above 1,500 V of V_{GM} in our case, as marked as a blue straight line) in natural logarithm is dominated by Fowler-Nordheim tunneling. Other regions in the voltage range are affected by thermionic and Schottky emissions. (b) Log-scale current fit taking into account the three components of thermionic, Schottky, and FN emissions. The resulting curve (black-dashed line) exactly matches the measurement data (see text for details).

The thermionic current is given by a well-known expression

$$J_{THc} = k_1 T^2 e^{\frac{-\theta}{k_B T}}, \tag{3.10}$$

where k_1 is the Richardson constant defined previously in Eq. (3.8).

Then, as the applied electric field increases, in the intermediate regime between thermionic emission and Fowler-Nordheim (FN) tunneling, a combination of the two effects occurs due to barrier lowering by the applied field. This intermediate region is where Schottky emission [74] plays a role for electron emission via modifying thermionic emission in the region where the electric field is not negligible, but it is not strong enough to cause FN tunneling:

$$J_{Sc} = k_1 T^2 e^{-\frac{\theta - \sqrt{\frac{Fe^3}{4\pi\varepsilon_0}}}{k_B T}}. \tag{3.11}$$

In this expression we can see how the applied electric field F, defined previously in Eq. (3.8), reduces the height of the barrier Θ at the surface. Finally, FN tunneling [52] takes over completely and dominates electron emission at fields above 10^7 V/m, which, in our setup, occurs when the applied voltage exceeds 1,500 V. FN tunneling is then modeled by the modified expression given previously in Eq. (3.7). A log-scale current fit taking into account the three components mentioned above is shown as a black-dashed line in the inset of Fig. 3-3 (b). When combined together, Eqs. (3.7), (3.10), and (3.11) give a complete and accurate account of field emission from the nanomembrane.

Chapter 4

Application of Diamond nanomembrane for detection of proteins

Ultrathin freestanding diamond membranes with large lateral dimensions are realized by straightforward etching methods based on semiconductor processing. The mechanical and electrical characteristics of the membranes are investigated by stress analysis, field emission measurement, and modeling as discussed in the previous chapters. With a minimal thickness of 100 nm and lateral dimensions over 400 μm the freestanding membranes offer extreme aspect ratios. In this chapter, ion detection by applying the diamond nanomembrane as a detector is demonstrated in a home-made MALDI-TOF system for Insulin (5,735 Da) and Cytochrome C (12,362 Da).

4.1 Operating principles of Diamond nanomembrane detector

The schematic configuration of MALDI-TOF analysis coupled with a diamond nanomembrane is illustrated in Fig. 4-1 (a) and (b). The detector assembly is located in front of the exit of time-of-flight tube as in common MALDI-TOF systems (see Fig. 4-1 (a)). In our case, the detector assembly has the freestanding diamond nanomembrane

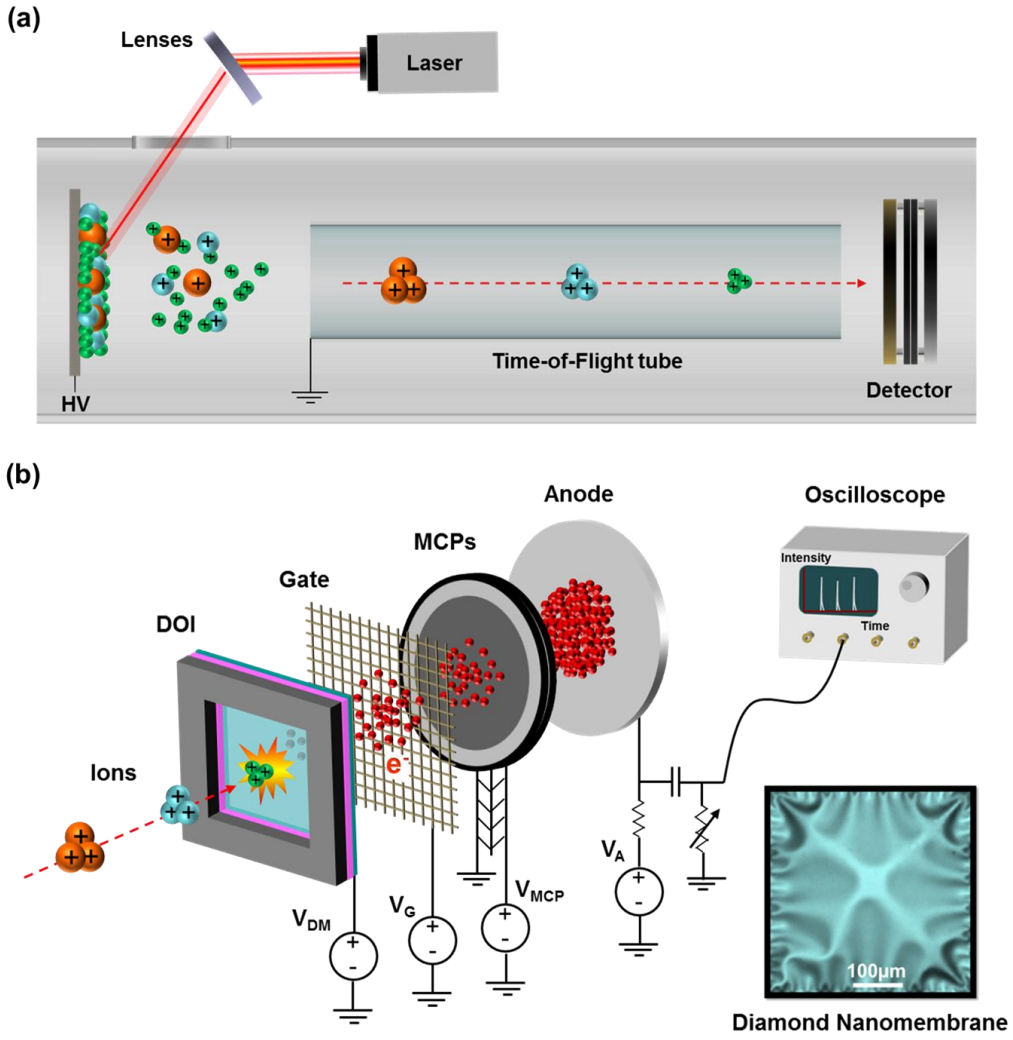

Fig. 4-1 The principle of operation for the diamond nanomembrane detector. (a) Schematic of a MALDI-TOF mass spectrometer. Proteins are desorbed and ionized by MALDI, followed by separation with mass to charge ratio during flight along the time-of-flight tube to the detector. (b) Schematic of the detector configuration and operation principle. The detector consists of a freestanding diamond nanomembrane (receiving the kinetic energy from the ions), an extraction gate, MCPs, and an anode. The electric field between the diamond nanomembrane and the extraction gate allows enhanced electron field emission by reducing the energy barrier for the electrons. MCPs amplify the number of electrons which pass through the extraction gate and arrive at the MCP. The electrons are collected in the anode, followed by tracing the signal in the time domain on an oscilloscope. Inset: optical microscope image of the 400 μm×400 μm freestanding 100 nm-thick *p*-type diamond nanomembrane used for measurement in this study (colorized). The buckling patterns in the membrane are generated by releasing of compressive residual stresses during etching of the substrate layers within the defined square window as discussed in previous chapters.

(lower right corner of Fig. 4-1 (b)) and the extraction gate built in front of a MCP input plate, as shown in Fig. 4-1 (b). Proteins on the sample holder are desorbed and ionized by a focused laser beam [3, 61, 62]. The ions are accelerated in a high DC field (~25 kV). They are separated by the mass to charge ratio while flying through the field free time-of-flight tube until they meet the detector. Finally, the ions impact on the backside surface of the freestanding diamond nanomembrane with a kinetic energy obtained by the initial accelerating voltage and the charges. About a half of the kinetic energy is transformed to thermal energy on the surface of the membrane due to loss in impact fragmentation and ejection [14]. This raises the temperature in the vicinity of the impact site and produces nonequilibrium phonons which carry thermal energy away from the location of impact. Thermal energy of these phonons is delivered to the electrons within the diamond nanomembrane and excites them to a higher energy allowing them to overcome the vacuum barrier and escape from the nanomembrane surface via field emission [26]. The field emission current is amplified by the microchannel plates (MCPs) via sequential cascade process of electrons inside MCPs and collected by the anode, followed by recording in an oscilloscope in real time as shown in Fig. 4-1 (b).

4.2 Detection of proteins

The application of freestanding diamond nanomembranes for detection of proteins is demonstrated in a home-made MALDI-TOF MS system with a vacuum level around 2.0×10^{-7} mbar as shown in Fig. 4-2. The membrane is mounted by attaching it on

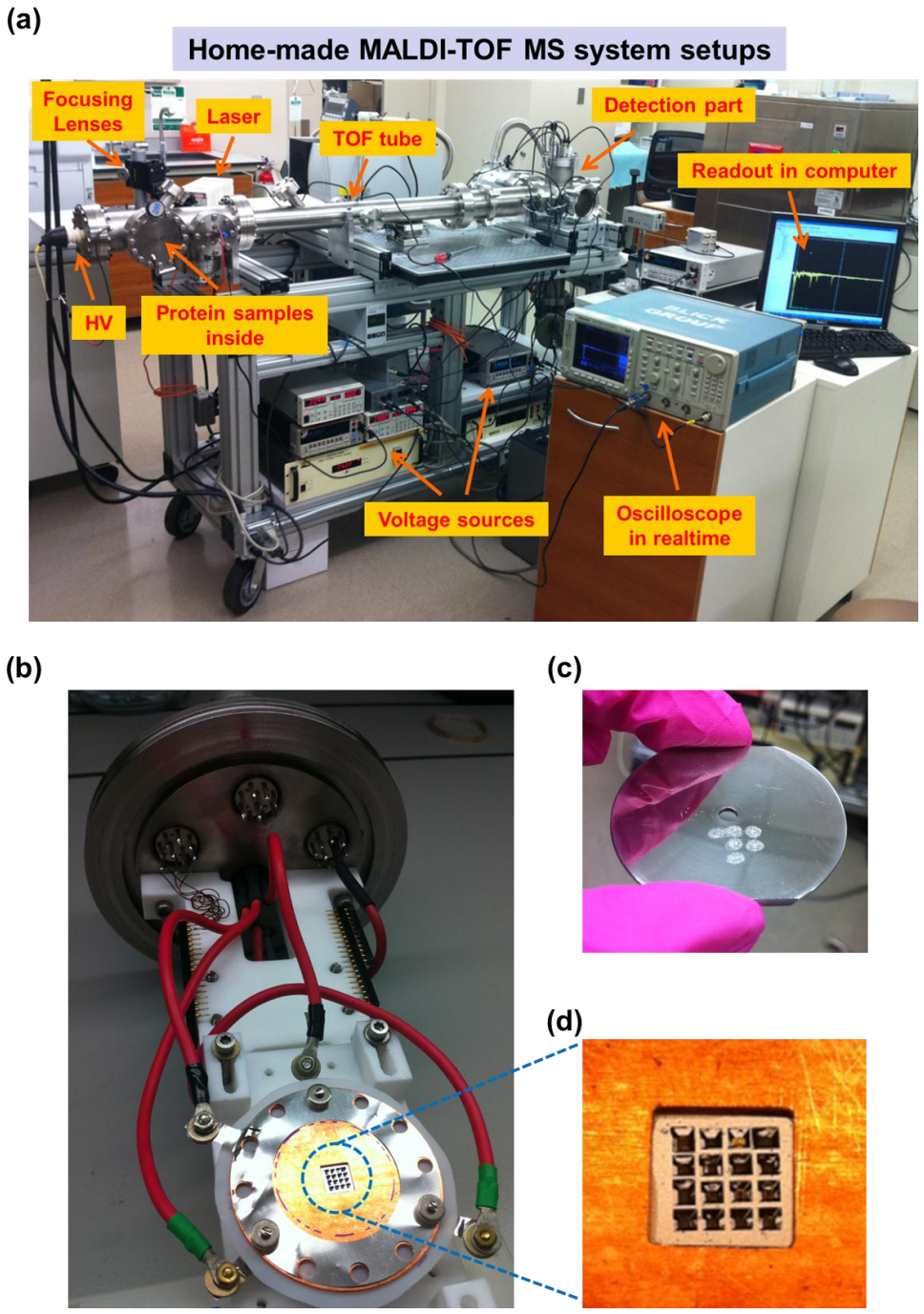

Fig. 4-2 Home-made MALDI-TOF MS system for ion detection. (a) Photograph of whole system setups. (b) Diamond nanomembrane detector mounted. (c) Protein sample plate with dried droplet spots of protein mixture and matrix. (d) Magnified image of the backside of the device with an intact diamond nanomembrane (light brown window in the first row and second column among sixteen windows).

a specially designed copper holder. A complete detector is assembled in a stack of membrane, sample holder, extraction gate grid, MCPs, and anode. The teflon holder with the detector is mounted in the chamber as shown in Fig. 4-1 (a) and Fig. 4-2 (b). Fig. 4-2 (d) shows the magnified image of a membrane sample (backside of the chip, etched side of substrate silicon) mounted on the detector. Among sixteen windows, one diamond nanomembrane survived during fabrication in this case is shown in the first row, second column. The teflon sheet cut with one hole is used for protecting ions going through broken windows of the sample chip. Insulin (5,735 Da) and Cytochrome C (12,365 Da) as proteins and Sinapinic acid (224 Da) (*Sigma Aldrich, U.S.A.*) as a matrix are used for demonstration. Fig. 4-2 (c) shows dried samples (mixture of protein and matrix) after mixing with droplet as solution on the protein sample plate. The focused laser beam shown in Fig. 4-2 (a) is fired at the dried droplet spot. The matrix absorbs the laser energy and is desorbed and ionized. Then, proton transfer occurs between the matrix and analyte protein molecule (in our case, Insulin and Cytochrome C), followed by charging the analyte proteins (mostly singly positive charged protein ions). For all cases of detection with Insulin and Cytochrome C, a high voltage in the ion source part is set to 25.02 kV and the voltage difference, V_{GM} between the diamond nanomembrane and the extraction gate is applied at 2,300 V. This considers the field emission characteristics previously discussed in Chapter 3.

4.2.1 Insulin

Ion detection with the freestanding diamond nanomembrane is demonstrated for

Insulin (5,735 Da, 100μM). Several results of mass spectra detected are shown in (a), (b), (c), and (d) in Fig. 4-3. All mass spectra are depicted as Amplitude (mV) versus *m/z* (Da). Since *m/z* describes the mass to charge ratio a singly charged ion has the same *m/z* value as its mass value while *n* times charged ion shows *m/z* value with mass/*n*. As shown in Fig. 4-3 the ions are mostly singly charged in the home-made MALDI. The peaks of the much lighter matrix than Insulin are first detected, then some fragments of proteins are detected and finally monomers, dimers, and trimers of Insulin (in Fig. 4-3 (b)) are detected. Mass spectra of MALDI normally show the fragment and incorporated compounds of same protein formed during the desorption process [22, 23]. However, the trimers and tetramers (in Fig. 4-3 (c)) of Insulin could not be detected only with the MCP detector. The fact that diamond nanomembrane detectors can detect trimers and tetramers of Insulin indicates the improved sensitivity.

As shown in Fig. 4-3 (c) the much lighter matrix, monomer, and tetramer of Insulin do not show reduced peak intensities as the mass is increased. This is typically seen as the limitation of MCP detectors discussed in Chapter 1. This results from the fact that the diamond nanomembrane detector response depends on kinetic energy of the ions. All ions (regardless of fragmentation and mixture) desorbed and ionized obtain the same kinetic energy. Then, the ions are deposited on the diamond nanomembrane with the same kinetic energy. The emitted electrons fly through the extraction grid and impinge on MCPs with same velocities owing to fixed same voltages between the extraction grid and MCP input plate as depicted in Fig. 4-1 (b). Therefore the output signal from the MCPs depends on the velocity of the incoming particles and hence is identical for ions with

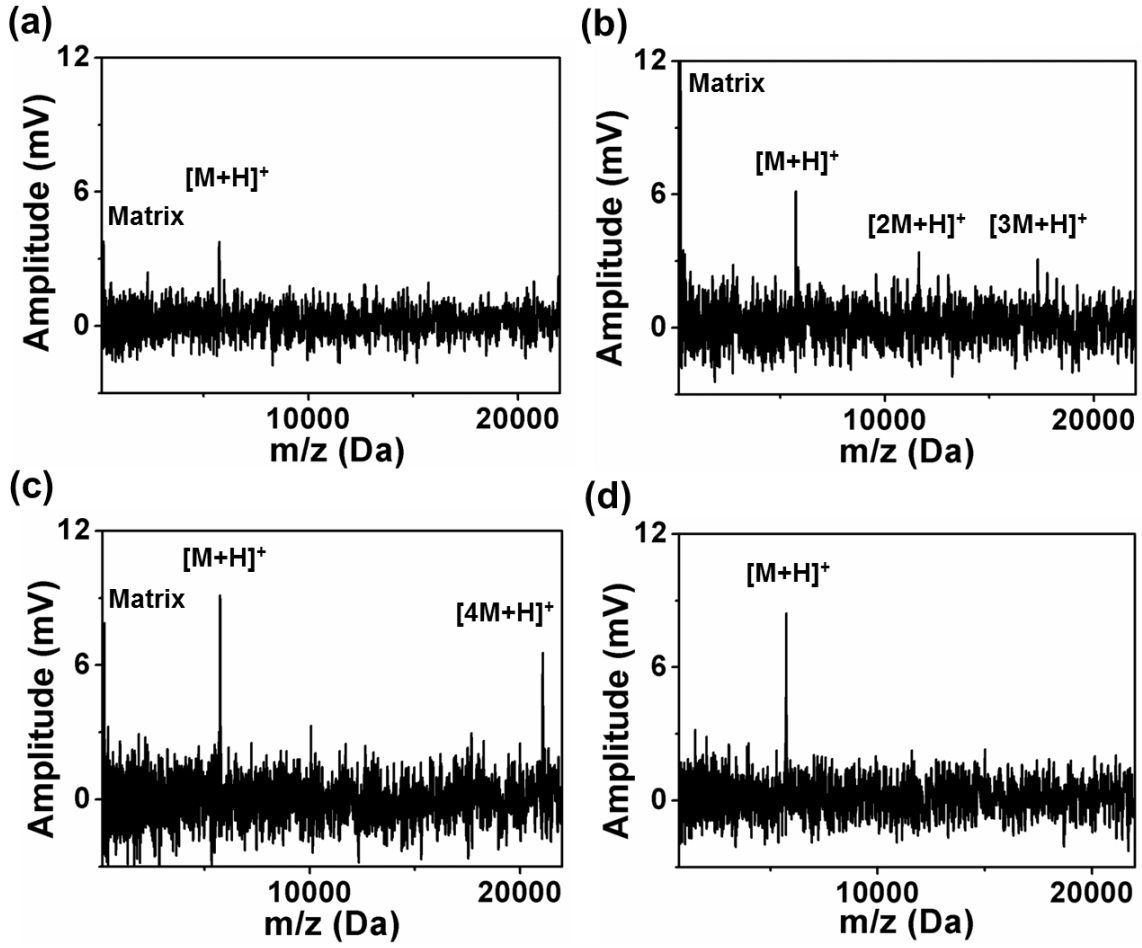

Fig. 4-3 Mass spectra obtained with the diamond nanomembrane detector for Insulin (5,735 Da) with a sinapinic acid matrix (224 Da). Mass spectra show peaks of dimers, trimers, and tetramers of Insulin as well as matrix and monomers of Insulin without large peak intensity reduction, which indicates improved sensitivity of the diamond nanomembrane detector.

different mass. This phenomenon is the beneficial characteristic of the nanomembrane detector [24-26].

4.2.2 Cytochrome C

Ion detection with the freestanding diamond nanomembrane is also demonstrated

for Cytochrome C (12,362 Da) with the same concentration of 100 µM as for Insulin. Several mass spectra are detected as shown in Fig. 4-4 (a) and (b). All operating conditions such as laser intensity, high DC voltage values, and membrane voltages, grid, and MCPs are fixed at the same values as in case of Insulin. To avoid loss of data in the spectra due to the lager time-of-flight of Cytochrome C and to obtain more data points, the signals from the matrix and small masses are pre-removed via a delayed run (60 µs) of the oscilloscope. (a) and (b) show the peaks of Cytochrome C detected with amplitude (mV) versus *m/z* (Da).

In terms of peak intensity, the signal in (b) is obtained with a better peak intensity than that in (a). The peak intensities of Cytochrome C are similar to those for Insulin shown in Fig. 4-3 even though Cytochrome C has much higher mass than Insulin. As discussed in the previous section (4.2.1), these phenomena result from characteristics of nanomembrane detectors being dependent on kinetic energy rather than the velocity of the ions. Since all conditions are the same for both cases (Insulin and Cytochrome C), the kinetic energy finally transferred to the detector is the same leading to similar peak intensities even for larger ion masses. MCPs (sensitive to velocities of incoming particles [13]) experience impact of electrons with same velocities in both Insulin and Cytochrome C.

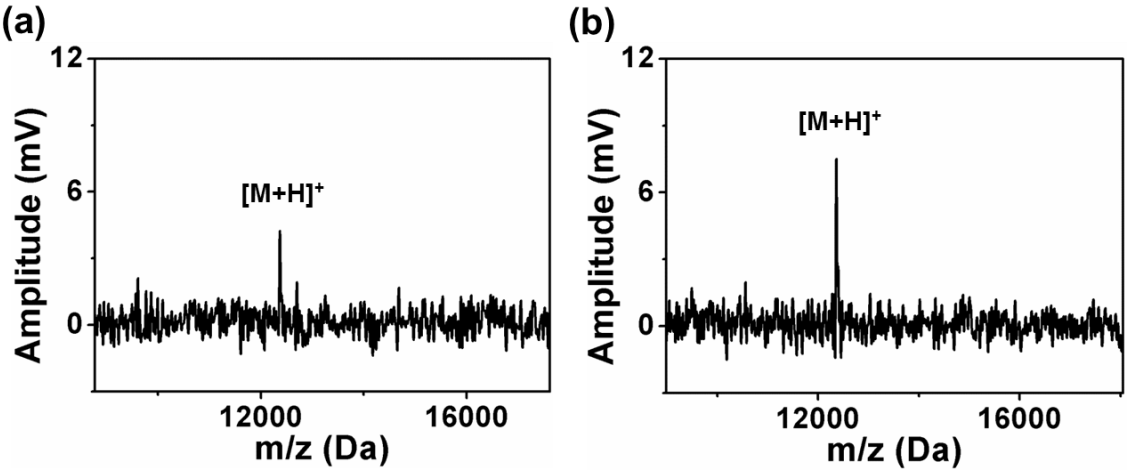

Fig. 4-4 Mass spectra obtained by the diamond nanomembrane detector for Cytochrome C (12,362 Da) with a sinapinic acid matrix. To protect loss of data points in spectrum due to the much larger mass (longer time-of-flight ranges) of Cytochrome C and to get more data points in large mass ranges of spectrums, the signals from the matrix and small mass ranges are pre-removed via delayed run (60μs) of the oscilloscope. Mass spectrums show similar peak intensities to those of Insulin indicating the improved detection sensitivity with diamond nanomembrane detector.

4.2.3 Analysis of mass spectra detected by Diamond nanomembrane

The peak intensities in the mass spectra of Insulin and Cytochrome C are similar to each other. Hence, the detection sensitivity is improved by the diamond nanomembrane detector, as discussed in the previous section. Two data sets obtained for those proteins are chosen for more analysis regarding the mechanism of detection. Fig. 4-5 shows the peaks for Insulin and Cytochrome C in (a) and (b), respectively. Insets in (a) and (b) are the magnified views of the peaks at the time-of-flight axis. The shape of the peak represents the sharp onset due to quasi-diffusive transport of phonons in the out-of-plane direction (normal to the surface of the membrane), and the exponential decay by the lateral heat diffusion along in-plane direction, as shown by the total aspect (red

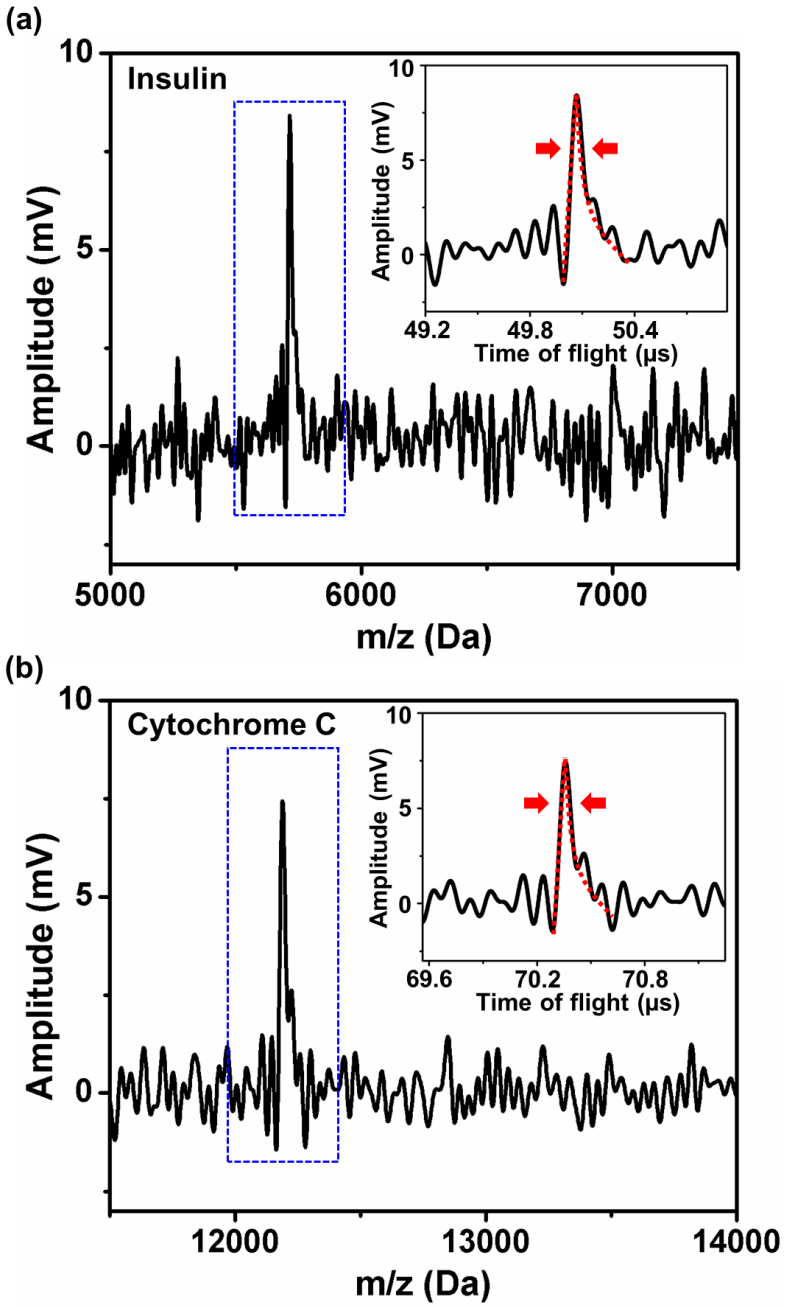

Fig. 4-5 Comparison of mass spectra obtained for Insulin (a) and Cytochrome C (b). Insets in (a) and (b) show the magnified views of the peaks at the time-of-flight axis. The rise time and the decay time constant at the peak of Insulin are 76.44 ns and 275.06 ns, respectively. The peak of Cytochrome C shows 73.36 ns and 265.09 ns. Overall aspects of the peaks are similar in both of Insulin and Cytochrome C. Owing to the time resolution being similar for all masses, the mass resolution ($m/\Delta m$) increases rather than decreases with increasing molecular masses. The mass resolution ($m/\Delta m$) obtained for Insulin and Cytochrome C appears to be ~350 and ~438, respectively.

dashed line) in the peak. The rise time and the decay time constants at the peak of Insulin are 76.44 ns and 275.06 ns, respectively. The peak of Cytochrome C shows 73.36 ns and 265.09 ns as the rise time and the decay time constants, respectively. As shown in Fig. 4-5, the amplitudes of the peaks, rise times, and decay time constants are very similar for both proteins because the concentration of proteins, initial accelerating DC voltage, and the dimension of membranes are fixed. Therefore, with the time resolution being similar for all masses, the mass resolution ($m/\Delta m$) increases rather than decreases with increasing molecular mass. Δm is defined as the full width at half maximum (FWHM) of the spectrum peak for the given mass (m). The mass resolution ($m/\Delta m$) obtained for Insulin and Cytochrome C is ~350 and ~438, respectively. These resolutions are even better than those obtained from Si_3N_4 0[24, 35] and Si nanomembrane detectors [26]. This underlines the potential for application of diamond nanomembrane detectors in MS.

The amplitude as well as the response times with onset and decay characteristics of the peaks depend on the mechanisms such as enhanced electron field emission by phonons (or heat) and phonon transport through the membrane. The analysis of these mechanisms is presented throughout the next sections.

4.3 Phonon-assisted field emission in diamond nanomembranes

Applying an electric field at the surface of the diamond nanomembrane lowers and thins the potential barrier, resulting in enhanced electron emission from the surface. In the case of ion detection the thermal energy transferred to the surface of the membrane via the impact of incoming ions contributes strongly to field emission leading to more

enhanced field emission via a thermionic component.

In more detail (schematic diagram of process is shown in Fig. 4-1 (b)), the nanomembrane is struck by the accelerated proteins from the MALDI-TOF apparatus. The proteins deposit their kinetic energy onto the membrane where the energy is absorbed as thermal energy, causing heating. The thermodynamics of the detection process control the observed tunneling current of electrons, which is measured by the detector anode. Inside the membrane, thermal energy is deposited on the back side by the impact of the proteins, followed by a rapid transport of that thermal energy through lattice vibrations (phonons) carrying the thermal energy across the membrane. Since the phonon velocity in diamond is very high (~ 17,500 m/s), the transit time of phonons across the 100 nm thick membrane is very short, on the order of 10 ps, and several orders of magnitude faster than either the duration of the impact of the protein cluster on the membrane or the response of the measured electron tunneling current. Following the fast transit time of quasi-ballistic phonons across the membrane, the temperature at the opposite surface of the membrane rises due to the presence of additional heat-carrying phonons and causes an increase in the tunneling current of electrons due to the combined thermionic emission and tunneling (field emission) effect.

The phonon assisted field emission current is driven by both the elevated temperature caused by the heating of the membrane combined with the field emission produced by the applied external field as shown in Fig. 4-6. The combination of thermionic emission and field emission is given by Eqs. (3.7), (3.10), and (3.11) where the presence of the $T^2 e^{-\frac{\theta}{kT}}$ term implies a strong dependence of the electron current on

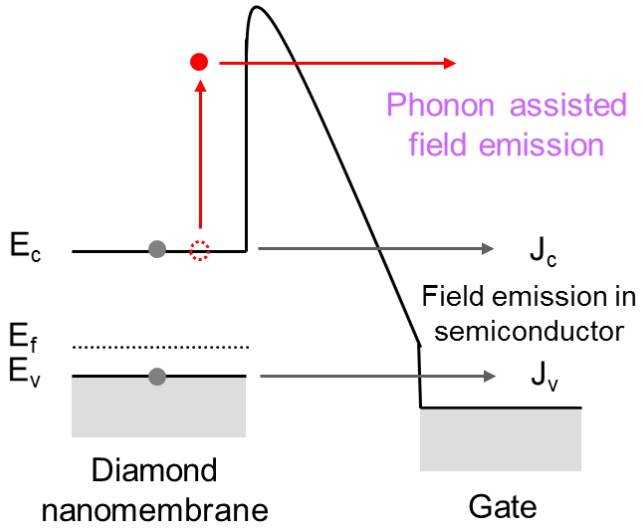

Fig. 4-6 Schematic energy diagram of phonon assisted field emission via heat generated by impacting ions onto the diamond nanomembrane surface. After absorbing thermal energy from the phonons generated by ion impact, electrons are excited to higher energy states. This leads to electrons overcoming and tunneling through the barrier more easily, which results in largely enhanced field emission. When electrons escape from the nanomembrane, they carry the energy amount resulting in cooling of the membrane.

temperature. The membrane is therefore a highly sensitive thermometer, producing a large tunneling current increase in response to the heating effect of the impacting proteins. As electrons leave the membrane by tunneling, they remove energy from the membrane, representing a cooling effect [75]. The total energy removed by the field emission process is $Q_{out}(T) = EJ(T,F)/e$, where e is the electron charge, E is the electron energy, and $J(T,F)$ is the temperature and field dependent total electron field emission current density, given by Eqs. (3.7), (3.10), and (3.11). Consequently, the membrane is heated on one side by the impact of the proteins and cooled on the opposite side by the energy extracted through the electron current via the combined thermionic and field emission

current.

In addition to the heat flux in the normal direction (out-of-plane) of the membrane, the accumulated heat also diffuses laterally in-plane. Normally the lateral heat diffusion process would dominate heat conduction, but because of the extremely large (more than 3 orders of magnitude) aspect ratio of the nanomembrane (thickness is 100 nm and lateral size is 400 μm or above) the heat diffusion in the lateral direction is severely limited. The thickness of the nanomembrane is smaller than the mean-free-path of phonons in diamond, which leads to a reduction of the thermal conductivity in the nanomembrane caused by scattering of phonons at the rough boundaries of the membrane. In addition, the thin nanocrystalline diamond utilized in our detector typically grows in columnar grains where the grains have diameters in the 3-5 nm range in the lateral direction, but are pillar-shaped and have no grain boundaries in the vertical (out-of-plane) direction [69]. The columnar grain structure means additional scattering of phonons will occur at the grain boundaries, affecting thermal transport in the lateral direction. Grain boundary scattering leads to a highly anisotropic thermal conductivity with the out-of-plane direction having nearly an order of magnitude higher thermal conductivity [68]. Out-of-plane heat flux is limited only by the phonon mean-free-path being equal to the thickness of the nanomembrane because of the boundary scattering at the atomic-level imperfections at the top and bottom surface. On the other hand, the in-plane thermal transport is limited by grain boundary scattering of phonons, which limits the phonon mean-free-path to $\Lambda = \langle d \rangle \frac{1+p}{1-p}$ where <*d*> is the average grain diameter, and *p* is the

so-called specularity factor which describes the probability of scattering at each grain boundary [76]. The specularity factor depends on the phonon wavevector q_p and the atomic scale roughness Δ at the grain boundary according to [77] $p = \exp\left(-4\Delta^2 q_p{}^2 \cos^2\Theta\right)$.

Consequently, the combination of thinness and columnar grain structure means thermal transport is predominantly ballistic in the normal (out-of-plane) direction, and strongly diffusive in the lateral direction. The large aspect ratio and low in-plane thermal conductivity also means that radiative heat losses, which are typically neglected due to being much smaller than convective heat diffusion, can contribute, with heat flux Q given by the Stefan-Boltzmann law $Q = \varepsilon\sigma A(T_h^4 - T_c^4)$ where σ is the Stefan-Boltzmann constant (5.67×10^{-8} W m^{-2} K^{-4}), A is the surface area, T_h and T_c are temperatures in the membrane and the environment (T_c = 300 K), and the emissivity ε is assumed to be 1.

We model the ballistic-diffusive transport of phonons in the nanomembrane by decomposing the problem into the normal and lateral direction, with the lateral heat diffusion being described by the heat equation with thermal conductivity calculated from the Boltzmann transport equation using full phonon dispersion and the phonon mean-free-path Λ. The details of our model are given in our previous work on silicon nanomembranes [26]. The resulting thermal conductivity value is 12 W/m/K at room temperature, in agreement with experimental data on nanocrystalline diamond films [68]. The lateral thermal conductivity in nanocrystalline diamond thin films is not strongly temperature dependent above room temperature because it is dominated by grain boundary scattering and inter-grain hopping conduction [78], which is largely

independent of temperature [70]. In the out-of-plane direction, the ballistic transport is no longer described by a thermal conductivity but rather by a ballistic conductance related to the phonon density of states (DOS) $D(\omega)$, phonon velocity v_p, and the transmission probability [79] and is given by

$$K(T) = \frac{1}{2\pi} \int_0^{\omega_{\max}} (\hbar\omega) v_p D(\omega) \frac{dN_0}{dT} \Xi(\omega) d\omega \tag{4.1}$$

where N_0 is the Bose-Einstein phonon distribution function and Ξ is the transmission function which depends on the phonon mean-free-path Λ and thickness t_M as $\Xi(\omega) = \Lambda(\omega) / \left[t_M + \Lambda(\omega) \right]$. In our case Ξ is assumed to be equal to 1 because the nanomembrane thickness of 100 nm is much smaller than the intrinsic mean-free-path in diamond. Finally, the impact of the proteins on the nanomembrane is treated as a heat source on the bottom side of the membrane having a Gaussian shape in time and space, while the cooling by field emission of electrons removes heat from the top, the two being connected to each other by ballistic phonon flux in the out-of-plane direction and to the boundaries of the membrane by lateral heat diffusion.

Therefore, the heat diffusion equation (HDE) must also be solved for the diamond nanomembrane with the combined effects of heating from the ion attack and the cooling due to field emission. First, the lattice thermal conductivity of the nanomembrane is obtained by solving the phonon Boltzmann transport equation in the steady-state relaxation time approximation. Then, the full phonon dispersion and all the relevant phonon scattering mechanisms are considered. The thermal conductivity tensor is obtained as a function of lattice temperature and both the in-plane and out-of-plane

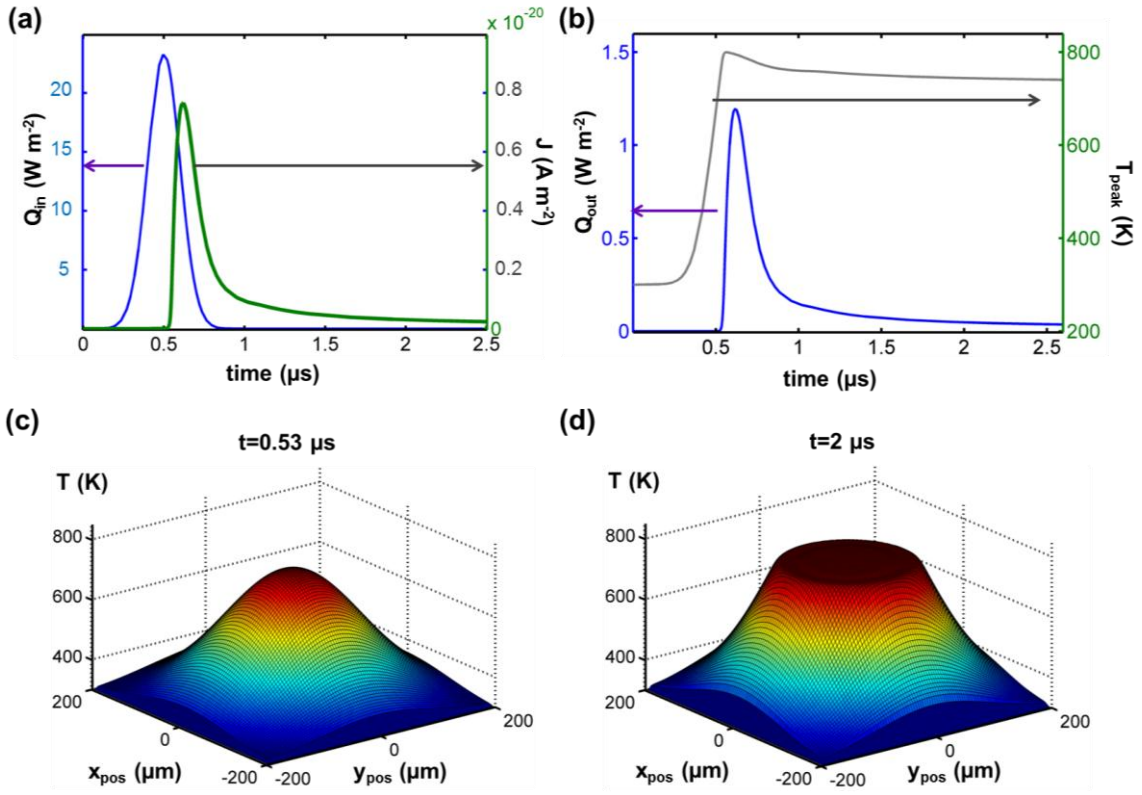

Fig. 4-7 Heat flux and temperature profile of the diamond nanomembrane. (a) shows a plot of the input heating Q_{in} caused by the impact of the proteins and the resulting field emission current density J as a function of time. Field emission leads to an effective cooling, represented by Q_{out} in (b) which limits the peak temperature of the membrane to about 800 K. The heating is initially strongest in the center, as shown by the peak in (c) obtained at t = 0.53 μs which is the onset of the field emission current. After the field emission begins to cool the nanomembrane, the temperature profile flattens in the middle, as depicted in (d) at t = 2 μs, at the tail of the field emission peak, when the peak temperature has dropped below 800 K.

components of the tensor and their respective contribution to thermal transfer within the nanomembrane.

Based on the thermal conductivity tensor for the diamond nanomembrane, the next step is to solve the HDE at all points throughout the nanomembrane given by

$$\rho C_p \frac{T}{t} = \nabla(k(T)\cdot\nabla T) + Q_{in}(t) - Q_{out}(T) \tag{4.2}$$

with the heating term $Q_{in}(t)$ (shown in Fig. 4-7 (a)) representing the heating effect of the kinetic energy deposited by the ions onto the backside of the nanomembrane and the cooling term $Q_{out}(T)$ (shown in Fig. 4-7 (b)) representing the energy loss due to the electrons escaping the front side of the nanomembrane via field emission. ρ and C_p is the density and the heat capacity of the material, respectively. The standard finite-difference method is used to discretize the Laplacian operator and the variable order adaptive method to advance the solution in time. The input term $Q_{in}(t)$ is also a function of position on the surface of the membrane as well as time. The heating effect by the incoming ion packet is assumed as a Gaussian function in both time and space as shown in Fig 4-7 (a).

Final modeling and numerical simulation for the output response via phonon-assisted field emission and heat flux after the high impact energy ion packet bombardment deposits its thermal energy on the backside of the diamond nanomembrane are performed with considering coupled effects of thermionic emission, heat diffusion, phonon scattering, cooling via phonon-assisted field emission and grain boundary effects through the membrane.

Results of the numerical simulation, in particular the electron current depicted in Fig. 4-7 (a), match the shape, the rise time of ~75 ns, and the fall time of ~275 ns exhibited in the measured waveforms (shown in Fig. 4-5 (a) and (b)), and show that the rise time is determined mainly by the heating process of the impacting proteins. The deposited kinetic energy heats the nanomembrane until it reaches a point where electron field emission increases and begins to cool the membrane, as evidenced by the delay

between Q_{in} and Q_{out} in Fig. 4-7 (a) and (b). Consequently, the rise time of ~75 ns depends primarily on the duration of the impact of the proteins and not on the transit time of the phonons across the membrane. The fall time is limited by the slower process of heat diffusion in the lateral direction—as the peak temperature T_{peak} (Fig. 4-7 (b)) in the nanomembrane falls, as shown in Figs. 4-7 (b)-(d), the heat loss (cooling) Q_{out} via the thermionic emission of electrons is rapidly quenched due to its super-exponential dependence on temperature, as given by Eqs. (3.7), (3.10), and (3.11). This strong temperature dependence of both J and Q_{out} explains the rapid initial drop in the electron tunneling current immediately following the impact of the proteins. What remains after J and Q_{out} decay (around ~1 μs in Fig. 4-7 (a) and (b)) is heat diffusion in the lateral direction and the radiative heat loss to the environment. Based on the simulations, we conclude that the combination of large aspect ratio, the small grain structure [68, 69] of the nanocrystalline diamond, and large phonon velocity combine to produce the rapid response by favoring the ballistic transport across the membrane and limiting the heat loss in the lateral direction.

4.4 Potential of Diamond nanomembrane as a detector

The application of diamond nanomembrane detectors to MS was demonstrated for Insulin and Cytochrome C in sinapinic acid matrix by integration into a home-made MALDI-TOF MS system. The mass spectra detected with the diamond nanomembrane show improved sensitivity and enhanced mass resolutions as compared to other types of nanomembrane detectors (Al/Si_3N_4/Al and silicon).

Although nanoscale-small grain sizes (~5 nm) of CVD ultrananocrystalline diamond (UNCD) form the grain structures inside the diamond nanomembrane as like pillars with 100nm in length and 5 nm in diameter leading to much degrading of thermal conductivity in-plane direction of the membrane, this type of diamond material can offer better sensitivity for detecting ions. In other words, due to those grain structures, heat is conducted across the membrane (out-of plane) well and along the membrane (in-plane) poorly, which directs most of the heat obtained by ion bombardment into out-of-direction and spread very little of it into lateral direction, but leading to more sensitive response with improved mass resolutions as an advantage.

In thermal point of view, these characteristics can make the response even from a smaller quantity of heat as long as it is localized. So a smaller cloud of molecules/proteins can be detected because all the heat goes straight across the membrane, not laterally. This localization effect generated due to the grain structure of UNCD can be the key to not only more sensitive detection, but also detection of smaller quantities or energies of proteins.

Finally, the properties of diamond material itself and chemical inertness as well as possibilities for improving the sensitivity and mass resolutions can offer potentials enough for more applications of diamond nanomembrane detectors in proteomics, including demonstration with various types of diamond nanomembranes and integration into commercial MALDI-TOF MS systems.

Chapter 5

Mass spectra obtained in application of a commercial MALDI-TOF MS system

The applicability of freestanding diamond nanomembranes was demonstrated as a detector in combination to a home-made MALDI-TOF MS system in the previous chapters. The principles of protein detection was modeled with numerical methods, which consider thermomechanical characteristics, physical boundary conditions of nanocrystalline diamond materials, and phonon transfer mechanisms. The resulting data explain an enhanced sensitivity and performance owing to the fast response time of CVD nanocrystalline diamond membrane. However, the home-made MALDI-TOF MS system itself has low quality of mass resolution leading to only a limited mass range. Thus a system with better performance is necessary for demonstrating the performance of diamond nanomembrane detectors for the high mass range. The coupling to a commercial MALDI-TOF MS system is necessary for demonstrating compatibility of diamond nanomembranes to commercial system. Therefore, we employed a Voyager DE-STR MALDI-TOF system (*Perseptive Biosystems*) in the following chapters.

The same chip with one survived nanomembrane (400 μm×400 μm freestanding 100 nm-thick *p*-type) is used. In addition various types of diamond nanomembranes are

applied with Voyager system. Insulin (5,735 Da), Cytochrome C (12,365 Da), Apomyoglobin (16,952 Da), Aldolase (39,212 Da), and Albumin (BSA, 66,430 Da) as proteins with diluted concentration (10 μM instead of 100 μM demonstrated in the previous chapter) and sinapinic acid (224 Da) (*Sigma Aldrich, U.S.A.*) as a matrix are used for demonstration.

5.1 Voyager DE-STR MALDI-TOF MS system setups

The Voyager DE-STR MALDI-TOF MS system is shown in Fig. 5-1. This commercial system has a built-in delayed extraction technology inside the system. With delayed extraction method, ions form in a field-free region, and then are extracted by applying a high voltage pulse to the accelerating voltage after a predetermined time delay instead of directly applying high DC voltage right after laser hitting as in home-made MALDI. By this technology, substantial energy loss from collision of ions in ion source and fragmentation of ions are reduced. Velocity focusing of ions controlled by variable-voltage grid in the ion source and the delay time applied to high accelerating voltage make it possible to accurately detect proteins of higher masses and at the lower concentrations. The load-lock system shown in Fig. 5-1 (a) provides high efficiency in mounting protein samples without venting the whole system. The protein sample plate (shown in (d)) with hydrophobic surface walls concentrates the protein sample spot into a small area. The custom-designed flange (shown in (b)) has several connectors for high voltage connections.

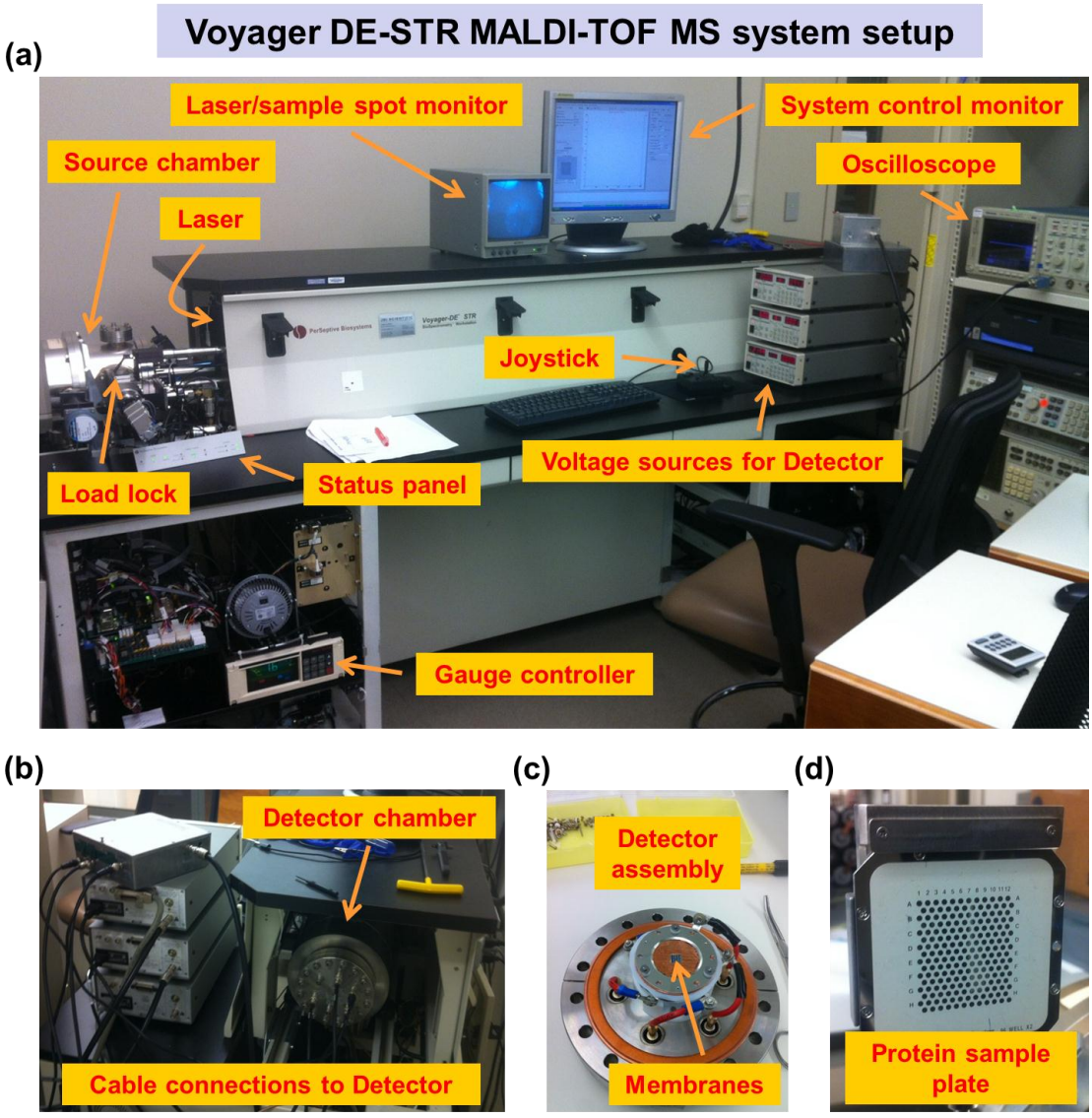

Fig. 5-1 Voyager-DE STR MALDI-TOF MS system setup. (a) Description of each part and element in the system setup. (b) Cable connections from voltage sources (for the detector) to the detector inside the detector chamber. (c) An image of the detector assembly with the sample chip. The detector assembly is mounted onto the vacuum flange. (d) 96×2 well protein sample plate. The sample plate with dried proteins is inserted into the source chamber via the load-lock system shown in (a). Overall performance in laser focusing, ion source part, separator, and vacuum system are improved as compared to a home-made MALDI-TOF system, which can make it possible to detect proteins in the lower concentrations and higher masses.

5.2 Freestanding diamond nanomembrane detectors demonstrated in detection

Several types of freestanding diamond nanomembranes for detection of proteins are demonstrated in Voyager DE-STR MALDI-TOF MS system: *(i)* Boron doped 400×400 μm^2 membrane with 100 nm thickness, *(ii)* Boron doped 400 μm diameter membranes with 500 nm thickness, *(iii)* undoped 400 μm diameter membranes with 300 nm thickness, and *(iv)* undoped 1 mm diameter membranes with 300 nm thickness. Insulin (5,735 Da), Cytochrome C (12,365 Da), Apomyoglobin (16,952 Da), Aldolase (39,212 Da), and Albumin (BSA, 66,430 Da) are used as proteins with diluted concentration to 10 μM (1/10 of 100 μM) in all cases. Sinapinic acid (224 Da) is used as a matrix with the same conditions as previous demonstration in a home-made MALDI-TOF MS system. The square nanomembrane in *(i)* is the same sample used in previous demonstration in the home-made MALDI-TOF MS system. Circular nanomembranes in *(ii)*, *(iii)*, and *(iv)* are fabricated by a company (*microFAB Service GmbH, Germany*), based on customized designs by the author of this thesis. Fabrication processes for those membranes are similar to the dry-etching method described in Fig. 2-1 (b).

5.2.1 Boron doped 400×400 μm^2 membrane with 100 nm thickness

Boron doped square type diamond nanomembrane (400×400 μm^2 membrane with 100 nm thickness, as shown in the inset of Fig. 4-1 (b)) is already demonstrated and gives promising results with the improved sensitivity for the detection of proteins such as

Insulin and Cytochrome C as discussed in the previous chapter. This device is now coupled to a Voyager DE-STR MALDI-TOF MS system for detection of proteins with higher mass and at lower concentration. The sample chip with one survived nanomembrane used for investigation in the previous chapter (shown in Fig. 4-2 (d)) is assembled and mounted onto the assembly stack, which is installed on the vacuum flange customized for demonstration in the system as shown in Fig 5-1 (c). For measurement, high accelerating voltage in ion source part is given at 23.5 kV and the voltage difference, V_{GM} between the diamond nanomembrane and the extraction gate is applied at 2,200 V.

Mass spectra detected for a wide mass range of proteins are shown in Fig. 5-2: we used concentrations of 10 μM for Apomyoglobin (16,952 Da), Aldolase (39,212 Da) and Albumin (BSA, 66,430 Da) (*Sigma Aldrich, U.S.A.*), while the matrix applied is sinapinic acid (224 Da). In the case of the equimolar (each 10 μM) mixture of Insulin and Cytochrome C shown in Fig. 5-2 (a), the peak intensities detected are independent of the ion mass as described in the previous chapter. Even for a wide mass range (a-d), all spectra appear to be independent of ion mass, which indicates the improved detection sensitivity of our diamond nanomembrane detector. The mass resolution ($m/\Delta m$) obtained for Apomyoglobin, Aldolase and Albumin is ~892, ~1,186, and ~1,443, respectively, i.e. mass resolution ($m/\Delta m$) increases with increasing molecular mass, which is explained as characteristics and strong points of diamond nanomembranes in the previous chapter.

The factor affecting the signal intensity is the concentration of proteins used. Since much diluted protein solutions provide a strongly reduced number of ions, the signals obtained by a 10 μM protein concentration are smaller and have worse signal-to-

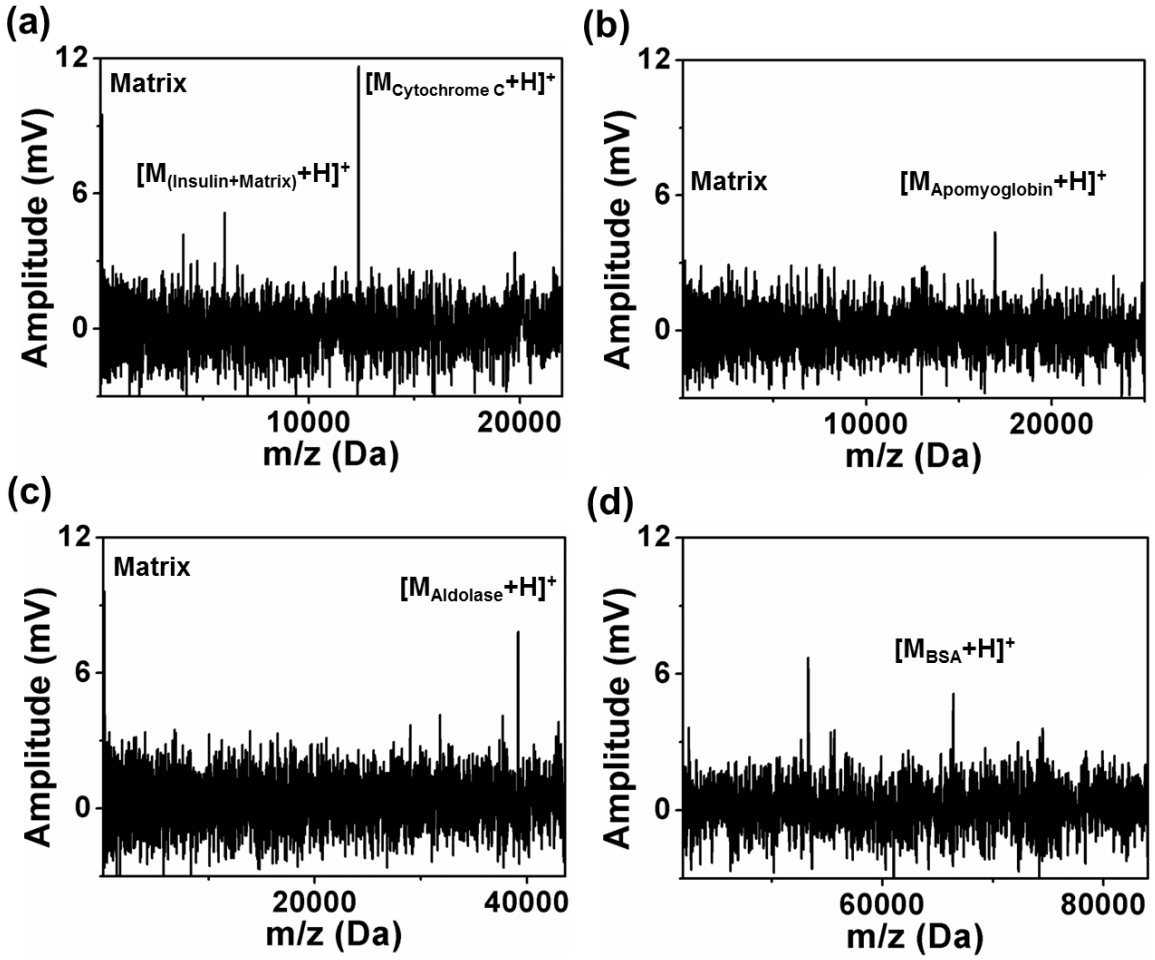

Fig. 5-2 Mass spectra obtained: for (a) equimolar (each 10 μM) mixture of Insulin (5,735 Da) and Cytochrome C (12,362 Da), (b) Apomyoglobin (16,952, 10 μM), (c) Aldolase (39,212 Da, 10 μM), and (d) Albumin (BSA, 66,430 Da) integrating the boron doped 400×400 μm^2 membrane (with 100 nm thickness) to a Voyager-DE STR MALDI-TOF MS system. In order to prevent the loss of data points in the spectra for Albumin the signal of the light matrix and other small molecules is removed using a delayed acquisition of the oscilloscope.

noise ratio as compared to a 100 μM concentration (See Figs. 4-3, 4-4, and 5-2).

5.2.2 Boron doped 400 µm diameter membranes with 500 nm thickness

Next demonstration is performed with Boron doped 400 µm diameter membranes (with 500 nm thickness) shown in Fig. 5-3 (a). Bulging profile (shown in Fig. 5-3 (b)) formed due to the compressive residual stress relaxed during releasing freestanding membranes from the substrate is investigated with the optical profilometer (*Zygo NewView 6300 white light interferometer, Zygo Corp., Middlefield, CT*). The maximum deformation of freestanding membranes is measured in around ± 4 µm (less than those of membranes with thinner thickness shown in Fig. 2-3) with bistable status (discussed in chapter 2.3) and without complicated wrinkle patterns (thinner membranes have larger local contribution of residual stresses [42-45]). Smoothly round bulging patterns can be from the lower residual stress and the thicker membrane structure against deformation [42-45]. Since some membranes of the sample chip were broken during voltage ramping up, three membranes (shown in Fig. 5-3 (d)) located in place with easy access for managing together are finally chosen and mounted onto detector assembly (shown in Fig. 5-3 (e)), followed by installing on a customized flange (shown in Fig. 5-3 (f)) to the detector chamber for demonstration. Other area except for three chosen membranes is covered by Mylar film (Mylar film has the much higher breakdown voltage than that of the teflon sheet), as shown in Fig. 5-3 (d) and (e). For this demonstration, a high accelerating voltage of the ion source part is chosen with 23.5 kV and the voltage difference, V_{GM} between the diamond nanomembrane and the extraction gate is applied at 2,400 V.

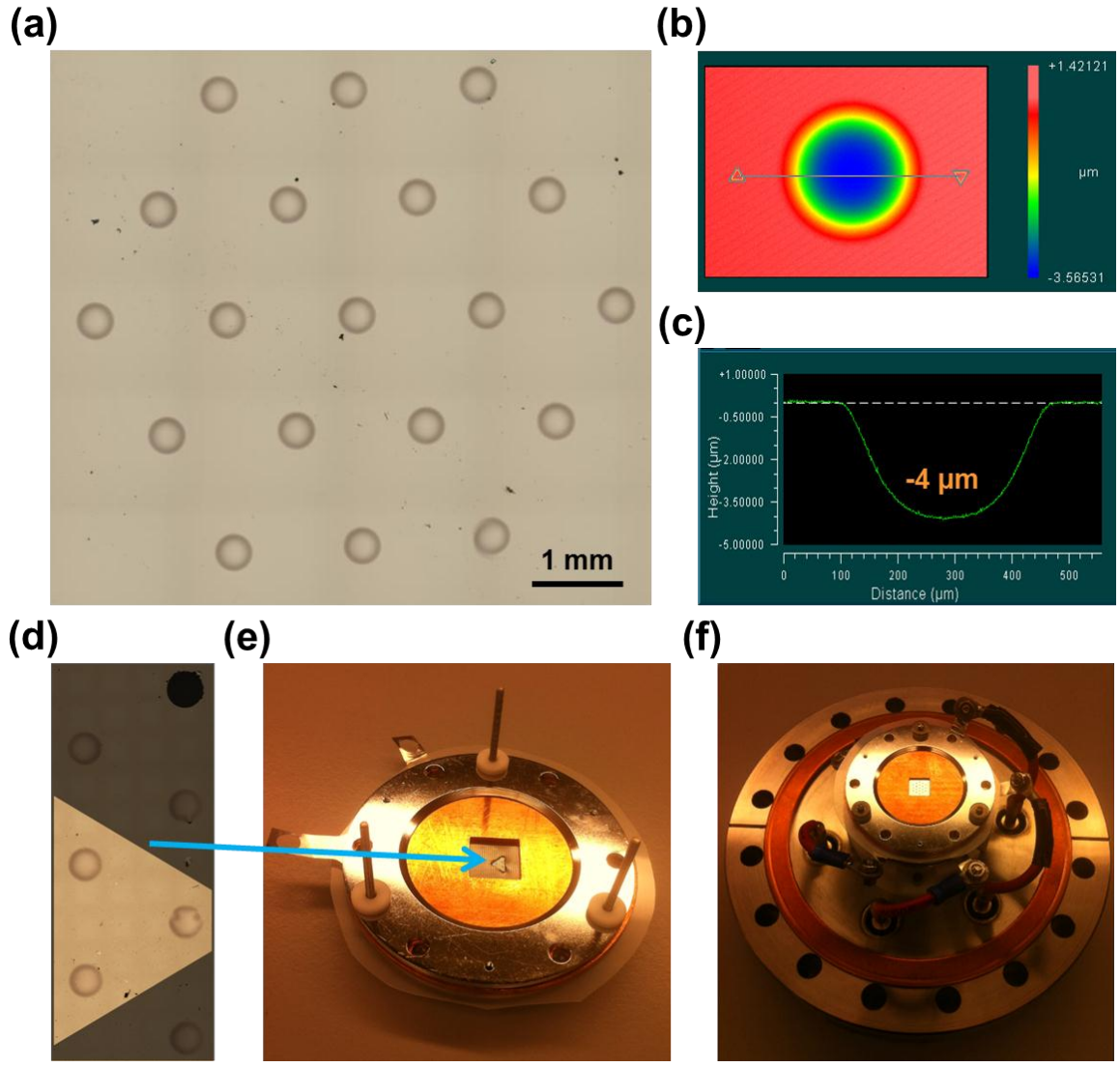

Fig. 5-3 Images for the sample device and detector assembly. (a) Original microscope image of fully survived freestanding boron doped 400 µm diameter membranes (with 500 nm thickness). (b) Color-scale profile of the bulging patterns and (c) deformation amplitudes (leveled for left and right end sides) obtained from line scans marked in the colored profiles measured in the optical profilometer. Freestanding nanomembranes have either of upward or downward deformation (here downward deformation of -4 µm is shown for one of the membranes). (d) A microscope image of three chosen membranes with covering other windows and areas with Mylar film (better insulator in several times than Teflon sheet) after breaking of some membranes which happened during ramping up voltages to the membranes. Three membranes are used finally for demonstration with opening to incoming ion attack as shown in (e). A detector assembly (f) is mounted onto a customized flange, followed by inserting to the detector chamber.

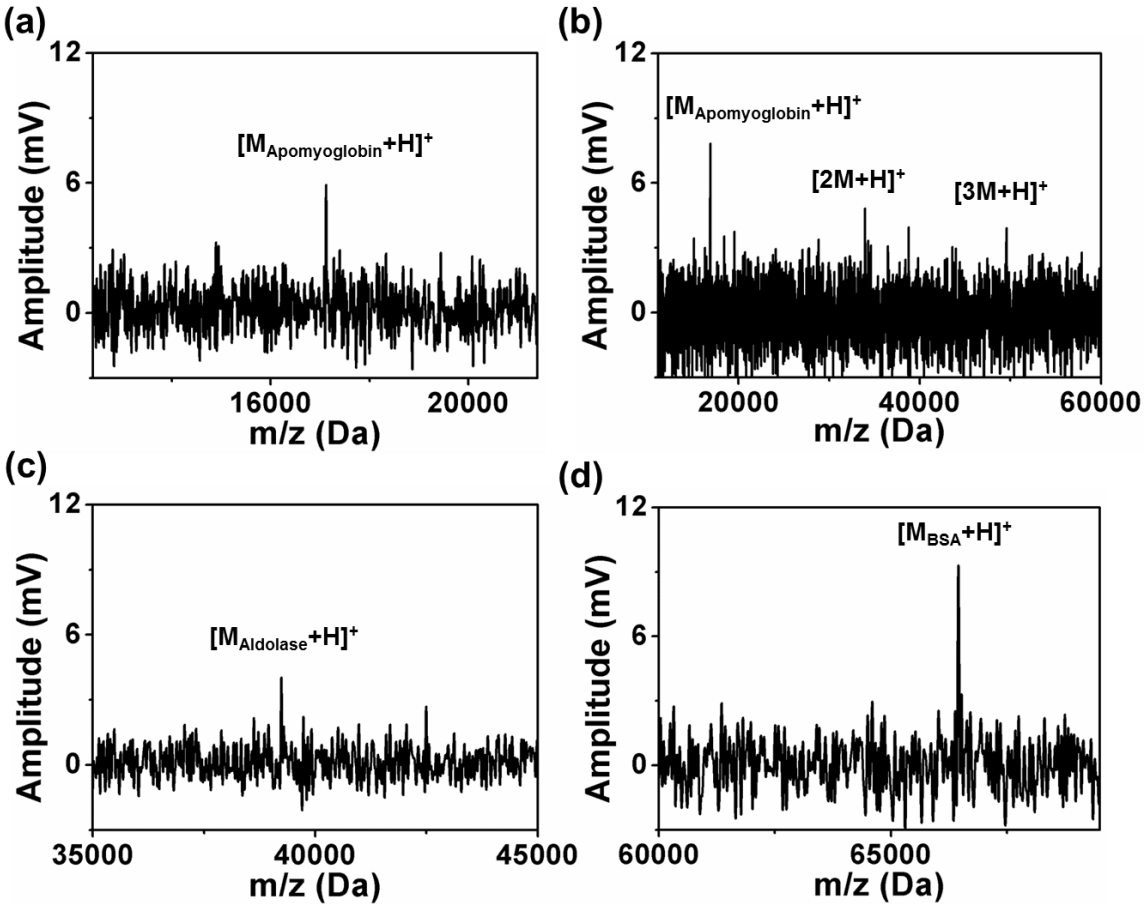

Fig. 5-4 Mass spectra obtained: for (a) and (b) Apomyoglobin (16,952, 10 µM), (c) Aldolase (39,212 Da, 10 µM), and (d) Albumin (BSA, 66,430 Da) with coupling of Boron doped 400 µm diameter membranes (with 500 nm thickness) to Voyager-DE STR MALDI-TOF MS system. In order to prevent the loss of data points in the spectra for all proteins the signal of the light matrix and other small molecules is removed using a delayed acquisition of the oscilloscope.

Mass spectra detected for a wide mass range of proteins are shown in Fig. 5-4: we also used concentrations of 10 µM for Apomyoglobin (16,952 Da), Aldolase (39,212 Da) and Albumin (BSA, 66,430 Da) (*Sigma Aldrich, U.S.A.*), while the matrix applied is sinapinic acid (224 Da). In the case of Apomyoglobin (16,952 Da) shown in Fig. 5-4 (a) and (b), monomers, dimers, and trimers as well as some fragments of Apomyoglobin

formed during desorption process are detected. Detection of several compounds of Apomyoglobin reveals enhancement of performance in diamond nanomembranes via coupling to commercial Voyager DE-STR system. Overall peaks (Fig. 5-4 (a)-(d)) of proteins detected have a little bit higher amplitudes as compared to those in Fig. 5-2 (b)-(d), which can be originated from a little bit increased effective areas for electron emission via using three circular diamond nanomembranes than previous case (shown in chapter 5.2.1). However, the thickness of nanomembranes, 500 nm does not permit large deformation of nanomembranes to the extraction gate (shown in Fig. 4-1 (b)), which can be easily learned from Eq. (2.2). In other words, even though membrane areas are now increased at around 2.4 times of the pervious device (in previous section, chapter 5.2.1**)** actual effective area for electron emission to the extraction gate with gate-driven deformation may be a little bit increased than that in previous device. In terms of comparison to each peak among different proteins**,** all spectra appear to be independent of ion mass, which indicates the improved detection sensitivity of our diamond nanomembrane detector regardless of coupled MALDI-TOF systems. The mass resolution ($m/\Delta m$) obtained for Apomyoglobin, Aldolase and Albumin is ~788, ~1,188, and ~1,660, respectively, i.e. mass resolution ($m/\Delta m$) increases with increasing molecular mass, as expected.

5.2.3 Undoped 400 μm diameter membranes with 300 nm thickness

This chapter presents demonstration with undoped 400 μm diameter membranes (with 300 nm thickness) shown in Fig. 5-5 (a). Buckling profile (shown in Fig. 5-5 (b))

formed due to the compressive residual stress relaxed during releasing freestanding membranes from the substrate is investigated with the optical profilometer (*Zygo NewView 6300 white light interferometer, Zygo Corp., Middlefield, CT*). The maximum deformation of freestanding membranes is measured around ± 5.75 μm (larger than those of membranes with larger thickness shown in Fig. 5-3 (b) and (c)) with bistable status (discussed in chapter 2.3). In terms of buckling patterns, more complicated wrinkle patterns appear due to larger local contribution of residual stresses via thinner membrane structures against initial deformation right after releasing [42-45] while previously used membranes show the smooth fundamental bulging mode in circular films (shown in Fig. 5-3 (b) and (c)).

All nanomembranes on the sample chip survived during all measurements, which can give the opportunity of full opening to incoming ion attack, followed by more effective areas for electron emissions as shown in Fig 5-5 (d). The sample chip with fully survived nanomembranes (total of 19 membranes, as shown in Fig. 5-5 (a) and (d)) is mounted onto the detector assembly (shown in Fig. 5-5 (d)), followed by anchoring onto a customized flange (shown in Fig. 5-5 (e)) inserted into the detector chamber for demonstration of protein detection. For measurement with this device, high accelerating voltage in ion source part is given at 23.5 kV and the voltage difference, V_{GM} between the diamond nanomembrane and the extraction gate is applied at 2,300 V.

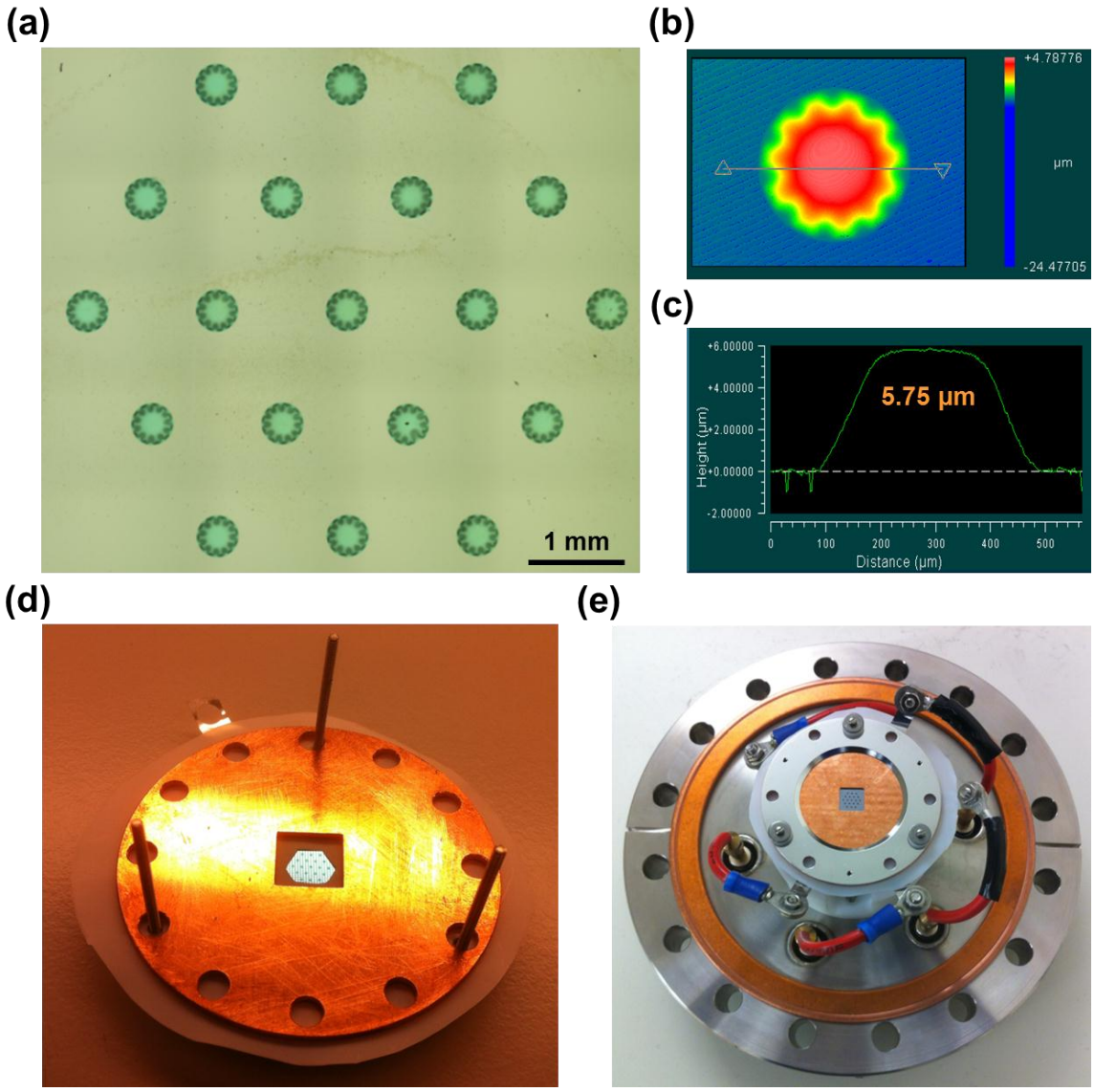

Fig. 5-5 Images for the sample device and detector assembly. (a) Original microscope image of freestanding undoped 400 µm diameter membranes (with 300 nm thickness). (b) Color-scale profile of the bulging patterns and (c) deformation amplitudes (leveled for left and right end sides) obtained from line scans marked in the colored profiles measured in the optical profilometer. Freestanding nanomembranes always have either upward or downward deformation (here upward deformation of 5.75 µm is shown for one of the membranes). For demonstration with this device, all nanomembranes are fully used owing to all surviving during ramping up voltages to the membranes. All surviving status of nanomembranes can give the opportunity of full opening to incoming ion attack, followed by more effective areas for electron emissions as shown in (d). A detector assembly (e) is mounted onto a customized flange, followed by inserting to the detector chamber.

Mass spectra detected for a wide mass range of proteins are shown in Fig. 5-6: we also used concentrations of 10 μM for Apomyoglobin (16,952 Da), Aldolase (39,212 Da) and Albumin (BSA, 66,430 Da) (*Sigma Aldrich, U.S.A.*), while the matrix applied is sinapinic acid (224 Da). In all cases, in order to prevent the loss of data points in the spectra for all proteins the signal of the light matrix, other small molecules, and multiplex compounds of proteins is removed using a delayed acquisition and the scale adjustment of the oscilloscope, which can focus on the targeted main proteins.

Fig. 5-6 (a) and (b) show the peaks obtained from Apomyoglobin (16,952 Da) and the fragments of it. The large main peak is also detected as shown in Fig. 5-6 (b), which reveals that effective electron emission happened at that moment in the given protein. For Apomyoglobin, Aldolase (39,212 Da) (shown in Fig. 5-6 (c) and (d)), and Albumin (BSA, 66,430 Da) (shown in Fig. 5-6 (e) and (f)) the overall protein peaks are clearly detected in terms of amplitudes and the signal to noise level.

Specially, overall yields for catching the protein signals (e.g. the numbers of events which proteins are detected at, not amplitudes detected) are enhanced for all proteins (normally, yields for catching signals become reduced as the protein mass increases. Otherwise, we can detect unlimited masses of proteins) owing to increased effective areas by increasing numbers of fully survived nanomembranes as compared to previously demonstrated devices. However, in terms of peak amplitudes, the effect of increased effective area of the detector is emerged only in the case of Apomyoglobin which shows the large peak amplitude shown in Fig. 5-6 (b).

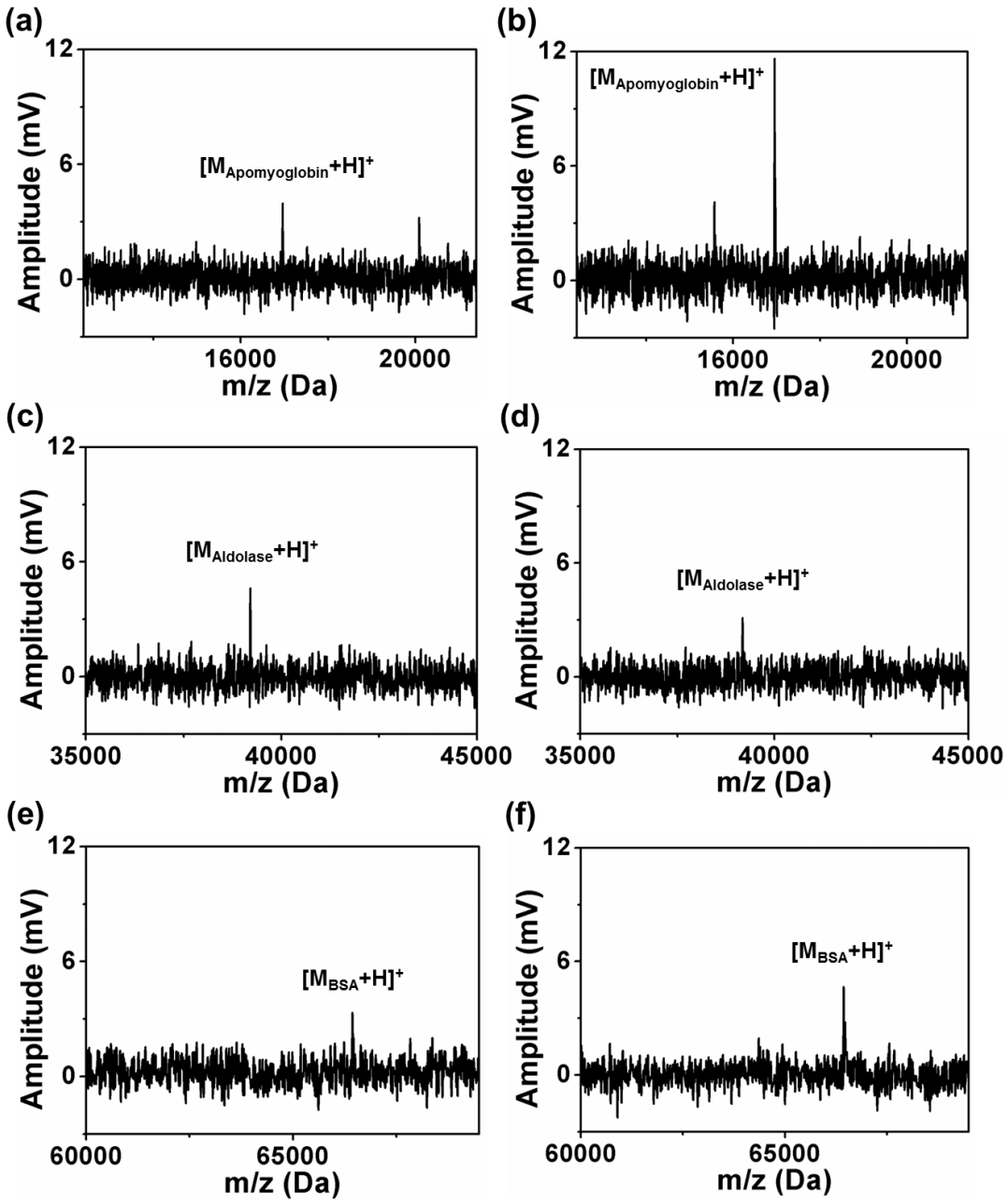

Fig. 5-6 Mass spectra obtained: for (a) and (b) Apomyoglobin (16,952, 10 µM), (c) and (d) Aldolase (39,212 Da, 10 µM), and Albumin (BSA, 66,430 Da) in (e) and (f) with coupling of fully survived freestanding undoped 400 µm diameter membranes (with 300 nm thickness) to Voyager-DE STR MALDI-TOF MS system. In order to prevent the loss of data points in the spectra for all proteins the signal of the light matrix and other small molecules is removed using a delayed acquisition of the oscilloscope. Overall yields for catching the protein signals are enhanced owing to increased effective areas by increasing numbers of fully survived nanomembranes.

In terms of comparison to each peak among different protein masses**,** all spectra (as shown in Fig. 5-6 (a)-(f)) appear to be independent of ion mass, which indicates the improved detection sensitivity of our diamond nanomembrane detector. The mass resolution ($m/\Delta m$) obtained for Apomyoglobin, Aldolase and Albumin is ~1,541, ~1,633, and ~1,718, respectively, i.e. mass resolution ($m/\Delta m$) increases with increasing molecular mass, as expected.

5.2.4 Undoped 1 mm diameter membranes with 300 nm thickness

This chapter finally presents mass spectra obtained with undoped 1 mm diameter membranes (with 300 nm thickness) shown in Fig. 5-7 (a). Buckling profile investigated with the optical profilometer is shown in Fig. 5-7 (b). The maximum deformation of freestanding membranes (as shown in Fig. 5-7 (c)) is measured in around ± 14.75 μm (with bistable status), which is larger than that of previously used membranes (in chapter 5.2.3) due to increased diameters with the same thickness. Initial deformation via buckling is affected largely by the dimensions of the structure as learned easily from Eq. (2.2) at the glance. As the diameter (or radius) increases with fixed residual stress (from the same thickness of the membrane) initial maximum deformation from bulging also increases. As shown in Fig. 5-7 (a)-(c), wrinkle patterns through the membrane become more complicated and sharper due to more nonlinear local contribution of residual stress via the larger surface dimension to thickness ratio [42-45]. From Fig. 5-3 (a), Fig. 5-5 (a), and Fig. 5-7 (a) in order, it is clearly shown that as the surface dimension to thickness ratios of the membranes increase the buckling patterns become more complicated and

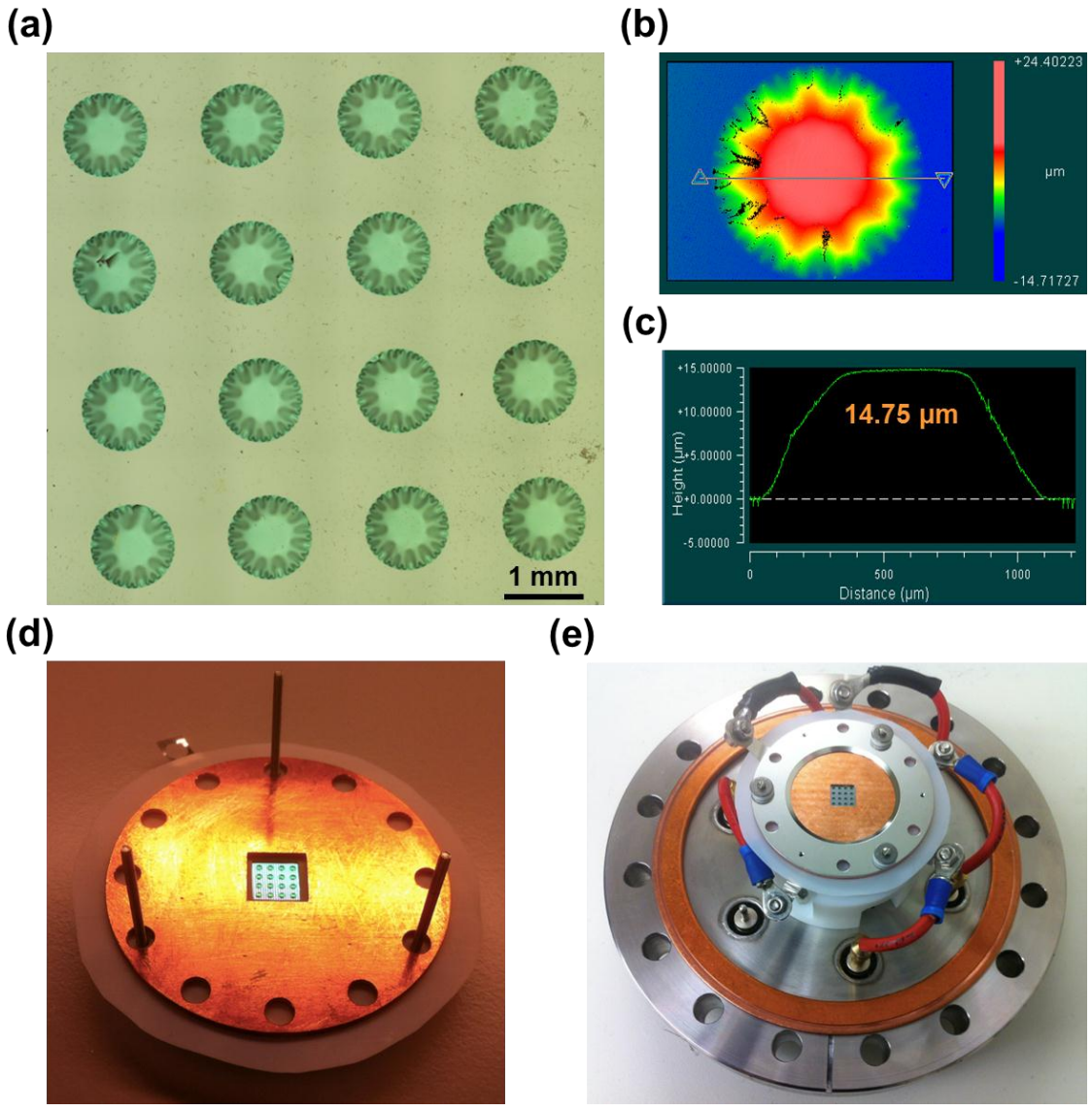

Fig. 5-7 Images for the sample device and detector assembly. (a) Original microscope image of fully survived freestanding undoped 1 mm diameter membranes (with 300 nm thickness). (b) Color-scale profile of the bulging patterns and (c) deformation amplitudes (leveled for left and right end sides) obtained from line scans marked in the colored profiles measured in the optical profilometer. Freestanding nanomembranes always have either upward or downward deformation (here upward deformation of 14.75 µm is shown for one of the membranes). For demonstration with this device, all nanomembranes are fully used owing to all surviving during ramping up voltages to the membranes as shown in (d). A detector assembly (e) is mounted onto a customized flange, followed by inserting to the detector chamber.

sharper with increased maximum deformations.

All nanomembranes in the sample chip demonstrated here survived even with larger surface dimensions during all measurement, which can give the opportunity of full opening to incoming ion attack, followed by much more effective areas for electron emissions as shown in Fig 5-7 (d). The sample device with all survived nanomembranes (total of 16 membranes, as shown in Fig. 5-7 (a) and (d)) is mounted onto the detector assembly (shown in Fig. 5-7 (d)), followed by attaching onto a customized flange (shown in Fig. 5-7 (e)) inserted into the detector chamber for demonstration in protein detection. All survived 16 nanomembranes in the sample chip are clearly shown in Fig. 5-7 (d), which can provide more electron emission via accepting more incoming protein ions onto the larger membrane areas. For measurement with this device, high accelerating voltage in ion source part is given at 23.5 kV and the voltage difference, V_{GM} between the diamond nanomembrane and the extraction gate is applied at 2,100 V.

Mass spectra detected for a wide mass range of proteins are displayed in Fig. 5-8. The concentrations of 10 μM is also used for Apomyoglobin (16,952 Da), Aldolase (39,212 Da) and Albumin (BSA, 66,430 Da) (*Sigma Aldrich, U.S.A.*), while the matrix applied is sinapinic acid (224 Da). In all cases, in order to prevent the loss of data points in the spectra for all proteins the signal of the light matrix, other small molecules, and multiplex compounds of proteins is also removed using delayed acquisition and the scale adjustment of the oscilloscope, which can focus on the targeted main proteins. Fig. 5-8 (a) and (b) show the peaks obtained from Apomyoglobin (16,952 Da). The large and clear main peaks are detected as shown in Fig. 5-8 (a) and (b), which are largest peaks obtained

for Apomyoglobin through demonstration of several types of diamond nanomembranes integrated into the Voyager DE-STR MS system. Those peaks show clear signal to noise levels. For Aldolase (39,212 Da) (shown in Fig. 5-8 (c) and (d)) and Albumin (BSA, 66,430 Da) (shown in Fig. 5-8 (e) and (f)) the overall protein peaks are clearly detected in terms of amplitudes and the signal to noise level. Overall yields for catching the protein signals, numbers of events which proteins are detected at, are much more enhanced for all proteins owing to increased effective areas from the number of fully survived membranes and larger surface dimensions as compared to previously demonstrated types of diamond membranes.

With comparison of each peak among different protein masses**,** although the peaks detected for Apomyoglobin show larger amplitudes in this demonstration, the overall aspects of spectra (as shown in Fig. 5-8 (a)-(f)) appear to be independent of ion mass, which indicates the improved detection sensitivity of our diamond nanomembrane detector. The mass resolution ($m/\Delta m$) obtained for Apomyoglobin, Aldolase and Albumin is ~1,334, ~2,242, and ~2,846, respectively, i.e. mass resolution ($m/\Delta m$) increases with increasing molecular mass, as expected.

Although direct comparison among each type of membranes demonstrated in this thesis is difficult due to the different number of membranes (the sample chips have different numbers of intact membranes per chip) and the different dimensions of the membranes (at least one parameter among total area or the thickness should be fixed for exact comparison), the sample described in this chapter (fully survived undoped 1 mm diameter membranes with 300 nm thickness) gave overall good performance (among the

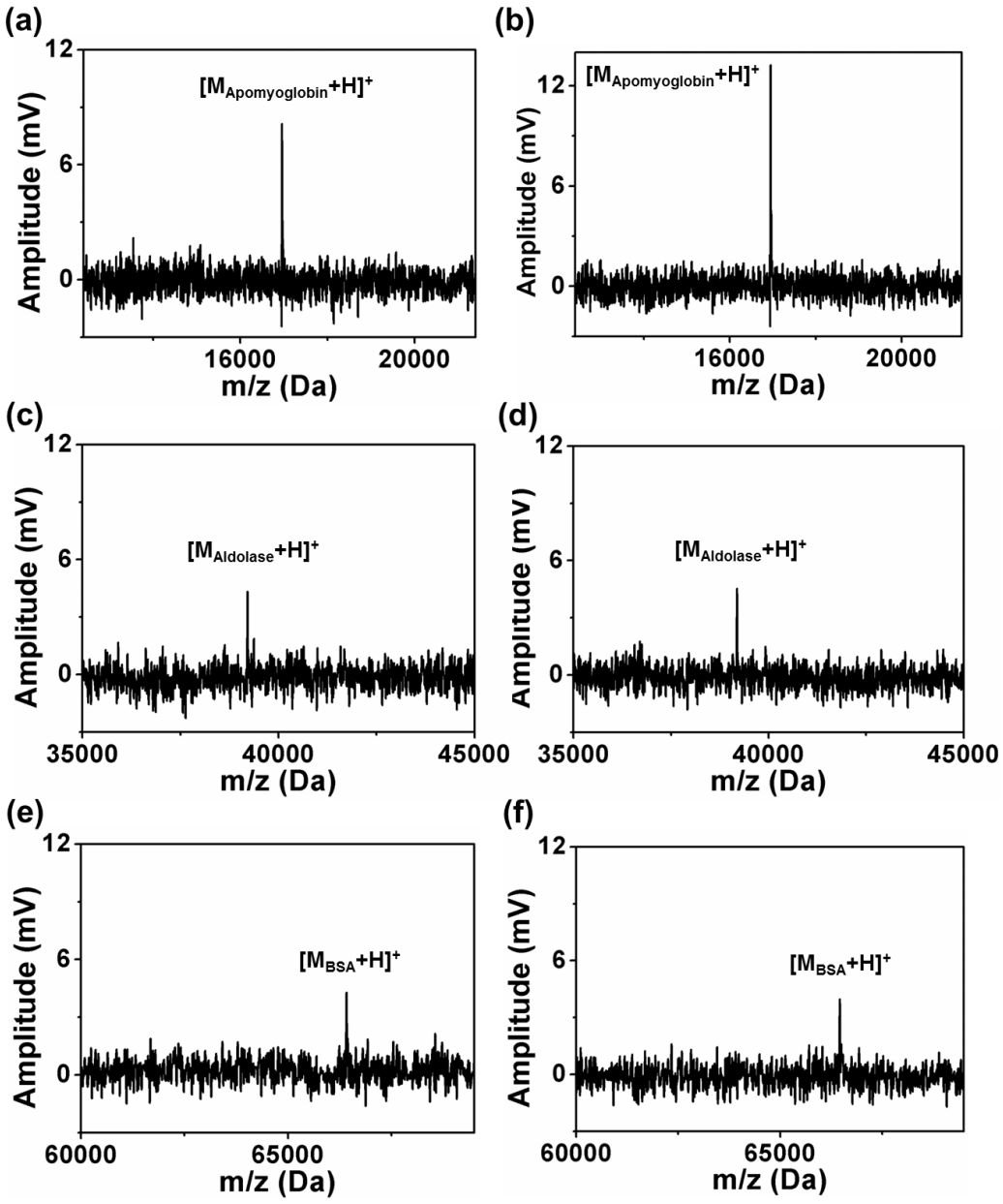

Fig. 5-8 Mass spectra obtained: for (a) and (b) Apomyoglobin (16,952, 10 µM), (c) and (d) Aldolase (39,212 Da, 10 µM), and Albumin (BSA, 66,430 Da) in (e) and (f) with coupling of fully survived freestanding undoped 1 mm diameter membranes (with 300 nm thickness) to Voyager-DE STR MALDI-TOF MS system. In order to prevent the loss of data points in the spectra for all proteins the signal of the light matrix and other small molecules is removed using a delayed acquisition of the oscilloscope. Overall yields for catching the protein signals are more enhanced owing to more increased effective areas by increasing numbers of fully survived nanomembranes and the larger area of nanomembranes than the previous device shown in Fig. 5-5 (a).

samples investigated through whole chapter 5) based on yields for detecting proteins, peak amplitudes, the signal to noise levels, and reliability of the membranes. This enhanced performance can stem from large total effective area against the thickness, which can provide effective electron emission owing to large surface area and more flexible bending of the membranes to the extraction gate with applied voltages. Although doping conditions cannot be compared directly in terms of performance (for this, the sample devices with exactly same dimensions and same number of survived membranes only except for doping conditions are needed for investigation), it is estimated that large effects to the performance are given by above mentioned factors rather than doping conditions since incoming proteins can give sufficient energies by impacting the surface for electrons to be emitted via phonon assisted field emission as discussed in details through chapter 4.3.

Chapter 6

Conclusions

Freestanding diamond nanomembranes were fabricated and investigated for applicability as field emitters. Various types of diamond nanomembranes were demonstrated as protein mass detectors by integration into MALDI-TOF MS systems. In this chapter the work presented in this thesis is summarized.

6.1 Summary and conclusions

We successfully demonstrated the fabrication of ultra-thin CVD grown diamond nanomembranes with extremely large cross sections, followed by the analysis of residual stress. We then investigated the field emission characteristics of freestanding diamond nanomembranes for validation of applicability as field emitters. The analytical work of field emission provided promising explanations for mechanisms of field emission, which include the mechanical and electrical response of the membrane and the electron emission mechanisms. We then employed the nanomembranes as mass detectors of various large proteins with coupling to the home-made MALDI-TOF MS system. We finally demonstrated various types of diamond nanomembranes for detection of various high mass proteins with diluted concentrations integrating the detector in a commercial

Voyager DE-STR MALDI-TOF MS system. From measurements, an enhanced performance was revealed for diamond nanomembranes with large total effective area against the thickness, which can provide effective electron emission owing to large surface area and more flexible bending of the membranes to the extraction gate with applied voltages.

Summarized presentations for mass resolutions ($m/\Delta m$) obtained in detection of the wide range of proteins with diamond nanomembranes are shown in Fig. 6-1. Fig. 6-1 (a) describes the mass resolution obtained applying the home-made MALDI-TOF MS system. Fig. 6-1 (b) shows the mass resolution obtained from the commercial Voyager DE-STR MALDI-TOF system. Since mass resolution can be also affected by other factors including the performance of the MALDI-TOF itself and conditions of the prepared proteins, the precise evaluation for the resolution values will need to be performed with considering those factors. Nevertheless, overall aspects of mass resolution obtained for a wide range of protein masses clearly show that mass resolution increases with increasing molecular mass (as shown in blue-dashed arrows), which is explained as characteristics and strong points of diamond nanomembranes as discussed in the previous chapters.

Analysis of data and numerical modeling showed the improved sensitivity and mass resolution (based on the fast response time), which originates from special thermomechanical characteristics of the nanocrystalline CVD diamond nanomembranes. These results offer the use of freestanding ultrathin- nanocrystalline CVD diamond nanomembrane as an outstanding detector for the detection of proteins with high mass in

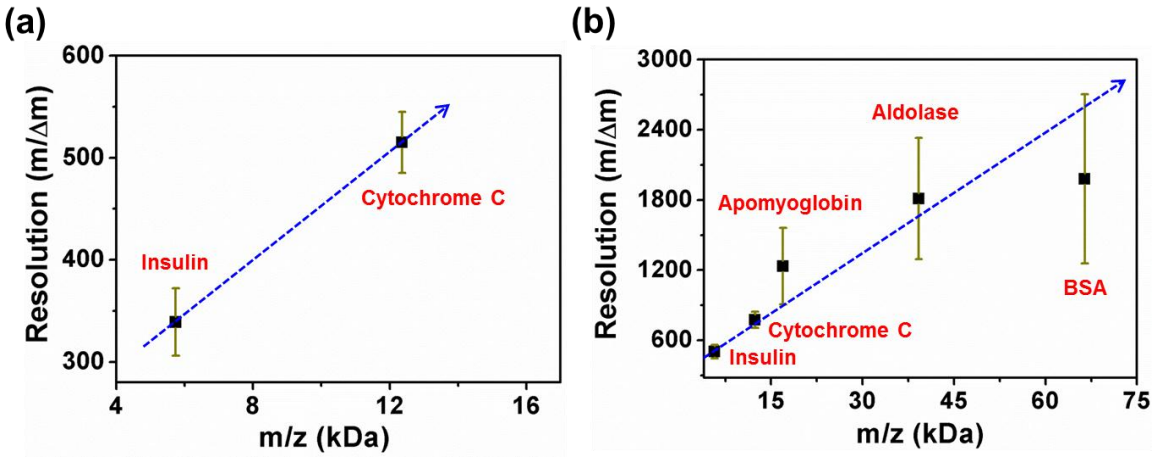

Fig. 6-1 Mass resolution (*m*/Δ*m*) obtained with diamond nanomembranes for various mass ranges: using the home-made MALDI-TOF MS system (a) and the commercial Voyager DE-STR MALDI-TOF system (b). Each square dot means the average values. Error bars in each square dot present the standard deviation.

proteomics. In addition to protein detection, it can be a good candidate as the device for any application which needs a fast response time in thermally driven detection via particle impact.

6.2 Recommendations for future work

The present work on freestanding ultrathin-nanocrystalline CVD diamond nanomembranes can be extended to investigate the following:

(i) Fabricate the sample chips with more intact diamond nanomembranes for 100 nm and 200 nm thicknesses, which can give large surface dimensions to thickness ratio for effective electron emission.

(ii) Fabricate more square diamond nanomembranes with various thicknesses via wet-etching method for more tests in commercial MALDI-TOF system and

comparison to circular diamond nanomembranes made by dry-etching method, which can give more insights for effects in performance by process methods, physical factors, and stress distribution.

(iii) Study the effects of doping/undoping conditions in performance for protein mass detection via demonstration with fixed physical dimensions of compared nanomembranes except for doping conditions.

(iv) Apply more diluted concentration of proteins and higher mass proteins in measurement for estimating the performance limit as a protein mass detector.

(v) Evaluate precise mass resolution values via obtaining more mass spectra by more measurements.

(vi) Extend coupled MS systems to other commercial MALDI-TOF systems or different types of MS systems, which can provide opportunities for checking more compatibility and taking advantage in performance of MS system itself.

(vii) Pursue more precise numerical calculations for investigating phonon assisted field emission according to various doping conditions and structure dimensions of diamond nanomembranes.

(viii) Execute more numerical calculations for virtually reproducing the buckling wrinkle patterns and studying local stress distribution contributed to the patterns.

(ix) Study the effects and performances in protein detection according to grain sizes in diamond layers with fabricating diamond nanomembranes with different grain sizes in diamond layer and demonstrating in detection of proteins.

Appendix A

Supplementary information

This chapter includes the supplementary information related to demonstration of diamond nanomembrane detectors for protein mass detection. Histograms obtained from collected mass spectra in demonstration with various types of diamond nanomembranes (boron doped 400×400 μm^2 membrane (100 nm thickness), boron doped 400 µm diameter membranes (500 nm thickness), undoped 400 µm diameter membranes (300 nm thickness), and undoped 1 mm diameter membranes (300 nm thickness)) and two MALDI-TOF MS systems (home-made MALDI-TOF MS system and commercial Voyager DE-STR MALDI-TOF MS system) described in chapters 4 and 5 are presented. The processes of preparing protein samples for measurement in MALDI-TOF MS systems are also introduced.

A.1 Histograms obtained from collected mass spectra

Histograms acquired from detection in wide mass ranges of proteins with various types of diamond nanomembranes in home-made MALDI-TOF MS system and commercial Voyager DE-STR MALDI-TOF MS system are presented in Fig. A-1, Fig. A-2, Fig. A-3, Fig. A-4, and Fig. A-5.

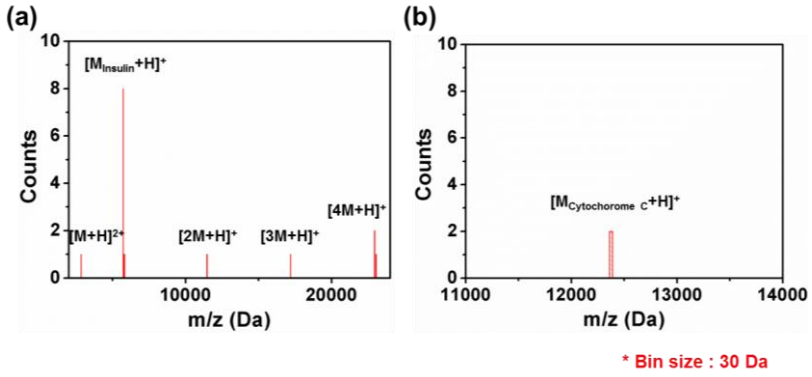

Fig. A-1 Histograms obtained from demonstration with boron doped 400×400 µm^2 membrane (100 nm thickness) in a home-made MALDI-TOF MS system. The concentrations of 100 µM is used for Insulin (5,735 Da), Cytochrome C (12,365 Da). The histograms show counts collected from protein masses detected in measurement with (a) Insulin and (b) Cytochrome. Bin sizes used for making histograms are 30 Da for all.

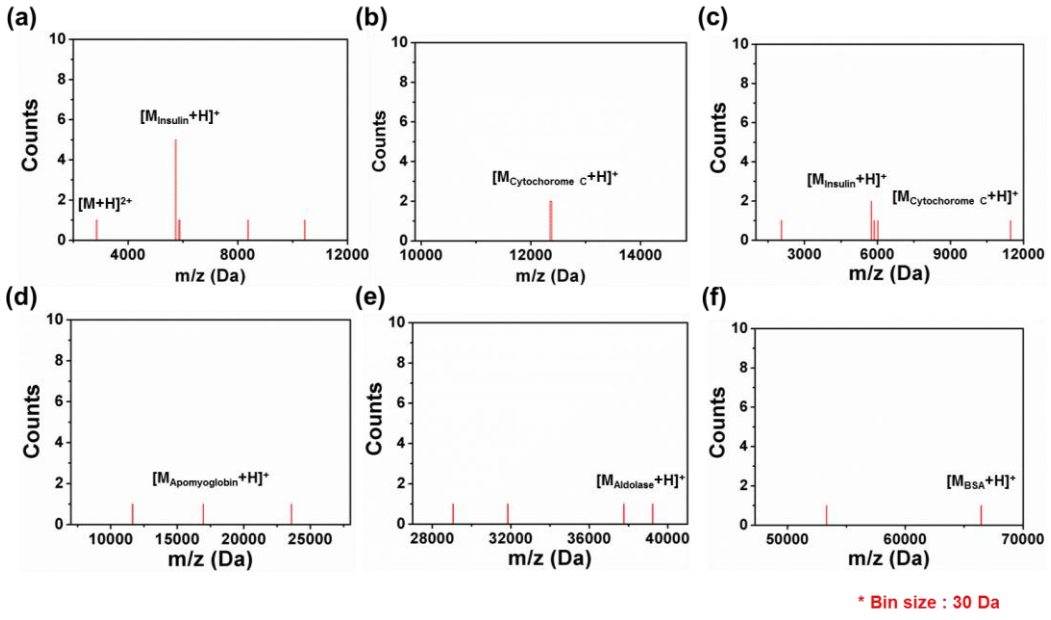

Fig. A-2 Histograms obtained from demonstration with boron doped 400×400 µm^2 membrane (100 nm thickness) in a commercial Voyager DE-STR MALDI-TOF MS system. The concentrations of 10 µM is used for (a) Insulin (5,735 Da), (b) Cytochrome C (12,365 Da), (d) Apomyoglobin (16,952 Da), (e) Aldolase (39,212 Da), and (f) Albumin (BSA, 66,430 Da). Equimolar (each 10 µM) mixture of Insulin (5,735 Da) and Cytochrome C (12,362 Da) is used for (c). The histograms show counts collected from protein masses detected in measurement for given proteins. Bin sizes used for making histograms are 30 Da for all.

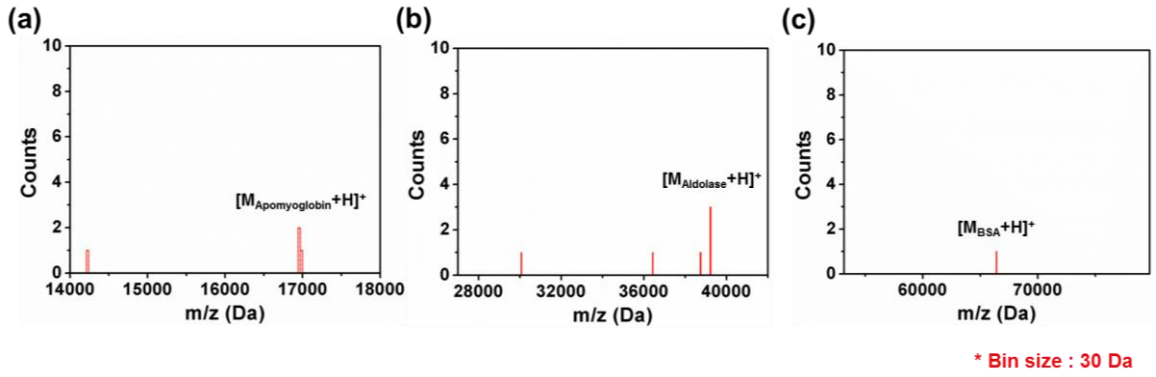

Fig. A-3 Histograms obtained from demonstration with boron doped 400 µm diameter membranes (500 nm thickness) in a commercial Voyager DE-STR MALDI-TOF MS system. The concentrations of 10 µM is used for (a) Apomyoglobin (16,952 Da), (b) Aldolase (39,212 Da), and (c) Albumin (BSA, 66,430 Da). The histograms show counts collected from protein masses detected in measurement for given proteins. Bin sizes used for making histograms are 30 Da for all.

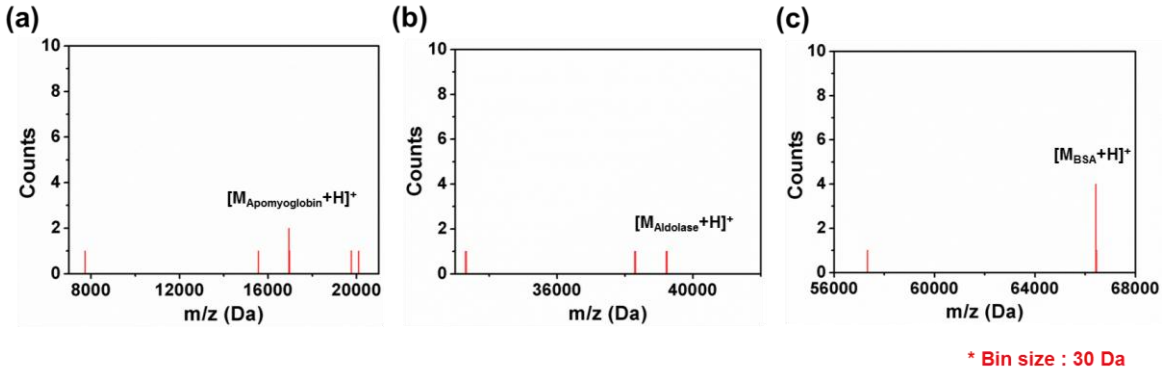

Fig. A-4 Histograms obtained from demonstration with undoped 400 µm diameter membranes (300 nm thickness) in a commercial Voyager DE-STR MALDI-TOF MS system. The concentrations of 10 µM is used for (a) Apomyoglobin (16,952 Da), (b) Aldolase (39,212 Da), and (c) Albumin (BSA, 66,430 Da). The histograms show counts collected from protein masses detected in measurement for given proteins. Bin sizes used for making histograms are 30 Da for all.

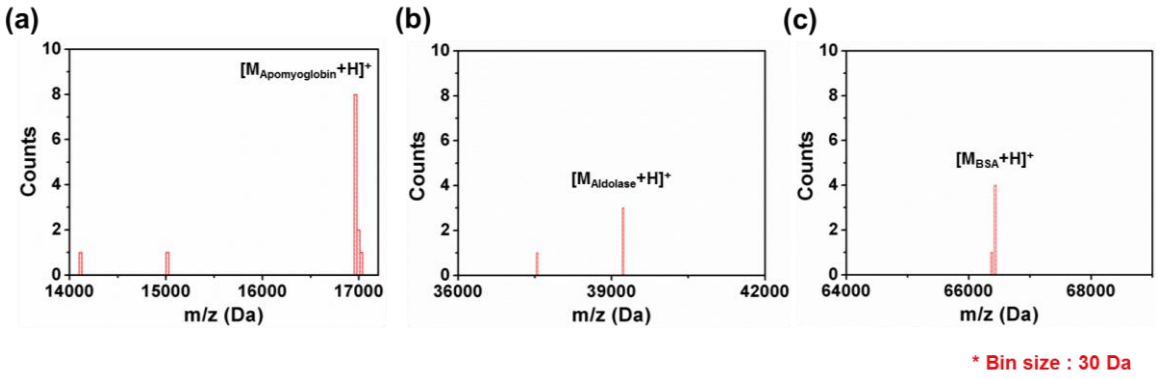

Fig. A-5 Histograms obtained from demonstration with undoped 400 µm diameter membranes (300 nm thickness) in a commercial Voyager DE-STR MALDI-TOF MS system. The concentrations of 10 µM is used for (a) Apomyoglobin (16,952 Da), (b) Aldolase (39,212 Da), and (c) Albumin (BSA, 66,430 Da). The histograms show counts collected from protein masses detected in measurement for given proteins. Bin sizes used for making histograms are 30 Da for all.

A.2 Preparation of protein samples

All the protein standards, matrix, and solvent for demonstration in detection of proteins are purchased from Sigma Aldrich, U.S.A. ProteoMassTM Protein MALDI-MS Calibration Kit includes the standard proteins, matrix, and solvent for preparing test samples in application to MALDI-TOF MS with diamond nanomembranes.

A 100 pmol/µl (100 µM) of each protein sample was prepared by dissolving 10 nmoles of it in 100 µl of 0.1 % trifluoroacetic acid (TFA) solution as a solvent. (Insulin was dissolved in the 1% TFA solution)

A 10 pmol/µl (10 µM) of each protein sample was obtained by dilution (1:9) of a 100 pmol/µl (100 µM) concentration with the appropriate solvent.

Equimolar (each 10 µM) mixture of two different proteins was prepared by mixing 20 µM solution of each protein together with the same volume of those solutions.

A 10 mg/ml concentration of 3,5-Dimethoxy-4-hydroxycinnamic acid (sinapinic acid) used as a matrix for the measurement was dissolved in 50% acetonitrile (ACN) in 0.05 % TFA solution.

For depositing protein samples and matrix onto the spot areas of the protein sample plate, 0.5 µl of matrix solution is first applied onto the target spot area, followed by removing applied matrix solution with leaving thin layer of matrix after 1 or 2 seconds. This process allows thin layer of matrix deposited onto the target spot area. After matrix deposited spots are dried, 0.5 µl of protein sample solution is applied onto the target spot area, followed by adding a further 0.5 µl of matrix solution before protein sample solution is dried. Once all applied solutions onto the target spot area finally become dry, the protein sample plate with target spots of sample proteins is ready for demonstration.

REFERENCES

[1] Aebersold, R. & Mann, M. Mass spectrometry-based proteomics. *Nature* **422**, 198-207 (2003).

[2] Fenn, J. B., Mann, M., Meng, C. K., Wong, S. F. & Whitehouse, C. M. Electronspray ionization for mass spectrometry of large biomolecules. *Science* **246**, 64-71 (1989).

[3] Karas, M. & Hillenkamp, F. Laser desorption ionization of proteins with molecular mass exceeding 10,000 Daltons. *Anal. Chem*. **60**, 2299-2301 (1988).

[4] Pandey, A. & Mann, M. Proteomics to study genes and genomes. *Nature* **405**, 837-846 (2000)

[5] Hager, J. W. A new linear ion trap mass spectrometer. *Rapid Commun. Mass. Spectrom*. **16**, 512-526 (2002)

[6] Guilhaus, M. Principles and instrumentation for TOF-MS. *J. Mass Spectrom*. **30**, 1519-1532 (1955)

[7] Wollnik, H. TOF-MS. *Mass Spectrom. Rev*. **12**, 89-114 (1993)

[8] Mamyrin B. A. Time-of-flight mass spectrometry (concept, achievements, and prospects). *International journal of Mass Spectrometry* **206**, 252-266 (2001)

[9] Schwartz, J. C., Senko, M. W. & Syka, J. E. A two-dimensional quadrupole ion trap mass spectrometer. *J. Am. Soc. Mass Spectrom*. **13**, 659-669 (2002)

[10] Marshall, A. G., Hendrickson, C. L. & Jackson, G. S. Fourier transform ion cyclotron resonance mass spectrometry: a primer. *Mass Spectrom. Rev*. **17**, 1-35 (1998)

[11] Martin, S. E., Shabanowitz, J., Hunt, D. F. & Marto, J. A. Subfemtomole MS and

MS/MS peptide sequence analysis using nano-HPLC micro-ESI fourier transform ion cyclotron resonance mass spectrometry. *Anal. Chem*. **72**, 4266-4274 (2000)

[12] Geno, P. W. *Ion detection in MS. In: Mass spectrometry in the Biological Sciences: A Tutorial* (Kluwer Academic Publ., Netherlands, 1992)

[13] Chen, X., Westphall M. S. & Smith, L. M. Mass spectrometric analysis of DNA mixtures: Instrumental effects responsible for decreased sensitivity with increasing mass. *Anal. Chem*. **75**, 5944-5952 (2003)

[14] Hilton, G. C., Martinis, J. M., Wollman, D. A., Irwin, K. D., Dulcie, L. L., Gerber, D., Gillevet, P. M. & Twerenbold, D. Impact energy measurement in time-of-flight mass spectrometry with cryogenic microcalorimeters. *Nature* **391**, 672-675 (1998)

[15] Frank, M., Labov, S. E., Westmacott, G. & Benner, W. H. Energy-sensitive cryogenic detectors for high-mass biomolecule mass spectrometry. *Mass Spectrom. Rev*. **18**, 155-186 (1999)

[16] Aksenov, A. A. & Bier, M. E. The analysis of polystyrene and polystyrene aggregates into the mega Dalton mass range by cryodetection MALDI TOF MS. *J. Am. Soc. Mass Spectrom*. **19**, 219-230 (2008)

[17] Ekinci, K. L., Huang, X. M. H. & Rouke, M. L. Ultrasensitive nanoelectromechanical mass detection, *Appl. Phys. Lett*. **84**, 4469-4471 (2004)

[18] Lassagne, B., Garcia-Sanchez, D., Aguasca, A. & Bachtold, A. Ultrasensitive mass sensing with a nanotube electromechanical resonator. *Nano Lett.* **8**, 2735-3783 (2008)

[19] Jensen, K., Kim, K. & Zettl, A. An atomic-resolution nanomechanical mass sensor. *Nature Nanotech*. **3**, 533-537 (2008)

[20] Naik, A. K., Hanay, M. S., Hiebert, W. K. Feng, X. L. & Roukes, M. L. Towards single-molecule nanomechanical mass spectrometry. *Nature Nanotech*. **4**, 445-450 (2009)

[21] Hanay, M. S., Kelber, S, Naik, A. K., Chi, D., Hentz, S., Bullard, E. C., Colinet, E., Duraffourg, L. & Roukes, M. L. Single-protein nanomechanical mass spectrometry in real time. *Nature Nanotech*. **7**, 602-608 (2012)

[22] Watson, J. T. & Sparkman, O. D. *Introduction to Mass Spectrometry: Instrumentation, Application, and Strategies for Data Interpretation*, 4th edn (John Wiley &Sons Inc., England, 2007)

[23] Hoffmann, E. d. & Stroobant, V. *Mass Spectrometry: Principles and Applications*, 3rd edn (John Wiley & Sons Inc., England, 2007)

[24] Park, J., Qin, H., Scalf, M., Hilger, R. T., Westphall, M. S., Smith, L. M. & Blick, R. H. A mechanical nanomembrane detector for time-of-flight mass spectrometry. *Nano Lett.* **11**, 3681-3684 (2011)

[25] Park, J., Kim, H. & Blick, R. H. Quasi-dynamic mode of nanomembranes for time-of-flight mass spectrometry of proteins. *Nanoscale* **4**, 2543-2548 (2012)

[26] Park, J., Aksamija, Z., Shin, H.-C., Kim, H. & Blick, R. H. Phonon-assisted field emission in silicon nanomembranes for time-of-flight mass spectrometry of proteins. *Nano Lett.* **13**, 2698-2703 (2013)

[27] Slack, G. A. Thermal conductivity of pure and impure silicon, silicon carbide, and diamond. *J. Appl. Phys*. **35**, 3460-3466 (1964)

[28] Chen, G. Nonlocal and nonequilibrium heat conduction in the vicinity of nanoparticles. *J. Heat Transfer* **118**, 539-545 (1996)

[29] Hahn, D. W. & Ozisik, M. N. *Heat conduction*, 3rd edn (John Wiley & Sons Inc., Hoboken, 2012)

[30] Balandin, A. A. Thermal properties of grapheme and nanostructured carbon materials. *Nature Mater*. **10**, 569-581 (2011)

[31] Privorotskaya, N., Liu, Y.-S., Lee, J., Zeng, H., Carlistle, J. A., Radadia, A., Millet, L., Bashir, R. & King, W. P. Rapid thermal lysis of cells using silicon-diamond microcantilever heaters. *Lab Chip* **10**, 1135-1141 (2010)

[32] Sumant, A. V., Auciello, O., Carpick, R. W., Srinivasan, S. & Butler, J. E. Ultrananocrystalline and nanocrystalline diamond thin films for MEMS/NEMS applications. *MRS Bulletin* **35**, 282-288 (2010)

[33] Spear, K. E. Diamond-ceramic coating of the future. *J. Am. Ceram. Soc*. **72**, 171-191 (1989)

[34] Wang, W. L., Polo, M. C., Sanchez, G., Cifre, J. & Esteve, J. Internal stress and strain in heavily boron-doped diamond films grown by microwave plasma and hot filament chemical vapor deposition. *J. Appl. Phys*. **80**, 1846-1850 (1996)

[35] Biswas, K. & Kal, S. Etch characteristics of KOH, TMAH and dual doped TMAH for bulk micromachining of silicon. *Microelectron. J.* **37**, 519-525 (2006).

[36] Yi, Z., Jifeng, W., Yuan, L. Research on wet etching at MEMS torsion mirror optical switch. *Proc. SPIE* **4902**, 593-599 (2002).

[37] Yan, G. *et al*. An improved TMAH Si-etching solution without attacking exposed aluminum. *Sens. Actuators, A* **89**, 135-141 (2001).

[38] Williams, K. R., Muller, R. S. Etch rates for micromachining processing. *J.*

Microelectromech. Syst. **5**, 256-269 (1996)

[39] Williams, K. R., Gupta, K. & Wasilik, M. Etch rates for micromachining processing-Part II. *J. Microelectromech. Syst*. **12**, 761-778 (2003)

[40] Wang, M. *et al*. Comparison of the chemical composition of boron-doped diamond surfaces upon different oxidation processes. *Electrochim. Acta* **54**, 5818-5824 (2009)

[41] Denisenko, A., Romanyuk, A., Pietzka, C., Scharpf, J. & Kohn, E. Surface damages in diamond by Ar/O_2 plasma and their effects on the electrical and electrochemical characteristics of boron-doped layers. *J. Appl. Phys*. **108**, 074901-1-074901-7 (2010)

[42] Kramer, T. & Paul, O. Postbuckled micromachined square membranes under differential pressure. *J. Micromech. Microeng.* **12**, 475-478 (2002)

[43] Ziebart, V., Paul, O. & Baltes, H. Strongly buckled square micromachined membranes. *J. Microelectromech. Syst.* **8**, 423-432 (1999)

[44] Evans, A. *et al*. Residual stress and buckling patterns of free-standing Yttria-stabilized-zirconia membranes fabricated by pulse laser deposition. *Fuel Cells* **12**, 614-623 (2012)

[45] Garbayo, I. *et al*. Electrical characterization of thermomechanically stable YSZ membranes for micro solid oxide fuel cells applications. *Solid State Ionics* **181**, 322-331 (2010)

[46] Madou, M. J. *Fundamentals of Microfabrication: The Science of Miniaturization*, 2nd edn (CRC Press, Boca Raton, 2002)

[47] Thornton, J. A. & Hoffman, D. W. Stress-related effects in thin films. *Thin Solid*

Films **171**, 5-31 (1989)

[48] Schomburg, W. K. *Introduction to Microsystem Design*, RWTH edn (Springer-Verlag, Berlin Heidelberg, 2011)

[49] Maier-Schneider, D., Maibach, J. & Obermeier, E. A new analytical solution for the load-deflection of square membranes. *J. Microelectromech. Syst.* **4**, 238-241 (1995)

[50] Malhaire, C., Didiergeorges, A., Bouchardy, M., Barbier, D. Mechanical characterization and reliability study of bistable SiO_2/Si membranes for microfluidic application. *Sens. Actuators A* **99**, 216-219 (2002)

[51] Jackson, J. D. *Classical Electrodynamics*, 2nd edn (John Wiley and Sons, New York, 1975)

[52] Fowler, R. H. & Nordheim, L. Electron emission in intense electric fields. *Proc. R. Soc. London, Ser. A* **119**, 173-181 (1928)

[53] Yamada, T., Yamaguchi, H., Okano, K. & Sawabe, A. Field emission properties of boron- and phosphorus-doped diamond. *New Diamond Front. Carbon Technol.* **15**, 337-347 (2005)

[54] Joseph, P. T. *et al*. On the mechanism of enhancement on electron field emission properties for ultrananocrystalline diamond films due to ion implantation. *J. Phys. D: Appl. Phys.* **42**, 1-6 (2009)

[55] Bozeman, S. P. *et al*. Electron emission measurements from CVD diamond surfaces. *Diamond Relat. Mater.* **5**, 802-806 (1996)

[56] Chen, C.-L., Chen, C.-S., Lue, J.-T. Field emission characteristic studies of chemical

vapor deposited diamond films. *Solid State Electron.* **44**, 1733-1741 (2000)

[57] Stratton, R. Theory of field emission from semiconductors. *Phys. Rev.* **125**, 67-82 (1962)

[58] Stratton, R. *Proc. Phys. Soc. B* **68**, 746-757 (1955)

[59] Chen, S.-Y. & Lue, J.-T. Temperature dependence of surface band bending and field emission for boron-doped diamond and diamond-like films. *New J. Phys.* **4**, 79.1-79.7 (2002)

[60] Miller, H. C. Values of Fowler-Nordheim field emission functions. *J. Franklin Inst.* **282**, 382-388 (1966)

[61] Wiley, W. C. & McLaren, I. H. Time-of-flight mass spectrometer with improved resolution. *Rev. Sci. Instrum.* **26**, 1150-1157 (1955)

[62] Tanaka, K. *et al*. Protein and polymer analyses up to m/z 100,000 by laser ionization time-of-flight mass spectrometry. *Rapid Commun. Mass Spectrom*. **2**, 151-153 (1988)

[63] Nottingham, W. B. Remarks on energy losses attending thermionic emission of electrons from metals. *Phys. Rev.* **59**, 906-907 (1941)

[64] Charbonnier, F. M., Strayer, R. W., Swanson, L. W. & Martin, E. E. Nottingham effect in field and T-F emission: Heating and cooling domains, and inversion temperature. *Phys. Rev. Lett*. **13**, 397-401 (1964)

[65] Bron, W. E., Levinson, Y. B. & O′Connor, J. M. Phonon propagation by Quasidiffusion. *Phys. Rev. Lett*. **49**, 209-211 (1982)

[66] Msall, M. E., Tamura, S., Esipov, S. E. & Wolfe, J. P. Quasidiffusion and the

localized phonon sources in photoexcited Si. *Phys. Rev. Lett*. **70**, 3463-3466 (1993)

[67] Siemens, M. E., Li, Q., Yang, R., Nelson, K. A., Anderson, E. H., Murnane, M. M. & Kapteyn, H. C. Quasi-ballistic thermal transport from nanoscale interfaces observed using ultrafast coherent soft X-ray beams. *Nat. Mater*. **9**, 26-30 (2010)

[68] Verhoeven, H., Reiβ, F. H. & Zachai, R. Influence of the microstructure on the thermal properties of thin polycrystalline diamond films. *Appl. Phys. Lett.* **71**, 1329-1331 (1997)

[69] Touzelbaev, M. N. & Goodson, K. E. Application of micron-scale passive diamond layers for the integrated circuits and microelectromechanical systems industries. *Diamond Relat. Mater*. **7**, 1-14 (1998)

[70] Liu, W. L., Shamsa, M., Calizo, I. & Balandin, A. A. Thermal conduction in nanocrystalline diamond films: Effects of the grain boundary scattering and nitrogen doping. *Appl. Phys. Lett*. **89**, 171915-1-3 (2006)

[71] Murphy, E. L. & Good, R. H. Thermionic emission, field emission, and the transition region. *Phys. Rev*. **102**, 1464-1473 (1956)

[72] Aksamija, Z. & Knezevic, I. Anisotropy and boundary scattering in the lattice thermal conductivity of silicon nanomembranes. *Phys. Rev. B* **82**, 045319 (2010)

[73] Mead, C. A. Operation of tunnel-emission devices. *J. Appl. Phys*. **32**, 646-652 (1961)

[74] Seitz, F. *Modern Theory of Solid*, McGraw-Hill Book Company, New York, 161-168 (1940)

[75] Chung, M. S. *et al*. New analysis of electron energy exchange and cooling in

semiconductors. *Appl. Phys. Lett*. **92**, 083505 (2008)

[76] Graebner, J. E., Reiss, M. E. & Seibles, L. Phonon scattering in chemical-vapor-deposited diamond. *Phys. Rev. B* **50**, 3702-3713 (1994)

[77] Aksamija, Z. & Knezevic. I. Thermal conductivity of $Si_{1-x}Ge_x/Si_{1-y}Ge_y$ superlattices: Competition between interfacial and internal scattering. *Phys. Rev. B* **88**, 155318 (2013)

[78] Braginsky, L., Lukzen, N., Shklover, V. & Hofmann, H. High-temperature phonon thermal conductivity of nanostructures. *Phys. Rev. B* **66**, 134203 (2002)

[79] Jeong, C., Datta, S. & Lundstrom, M. Thermal conductivity of bulk and thin-film silicon: A Landauer approach, *J. Appl. Phys*. **111**, 093708 (2012)